
Unterschrift des Betreuers



TECHNISCHE
UNIVERSITÄT
WIEN
Vienna University of Technology

DIPLOMARBEIT

Magnetic losses in soft magnetic materials

Ausgeführt am

Institut für Festkörperphysik

der Technischen Universität Wien

unter der Anleitung von

Univ.Prof. Dipl.-Ing. Dr.techn. Roland Größinger

durch

Monika Antoni

Pillersdorfgasse 6/10, 1020 Wien

Datum

Unterschrift (Student)

Abstract

Soft magnetic materials are important in modern networks used for the distribution of electrical energy. They are part of transformers and generators as core material for example. The efficiency of those transformers and generators is among other things limited by the fact that energy has to be used to change the magnetization of the material.

In the present work, the frequency dependence of the hysteresis loop on a wide variety of materials has been investigated. Those materials range from the standard electro steel base alloy $\text{Fe}_{97}\text{Si}_3$ to a nanocrystalline material. The measurements were performed using a self-built hysteresograph on ring shaped samples. It is crucial for measurements like this to use a well defined shape of the applied field $H(t)$ respectively $B(t)$. One of the goals of this work was to investigate the effect of the shape of $H(t)$ as well as $B(t)$. Hysteresis measurements were performed using sinusoidal $H(t)$, triangular $H(t)$ as well as triangular $B(t)$ and their frequency behaviour was compared. By numerical integration of the hysteresis area, the frequency dependence of the losses was evaluated.

The magnetisation reversal losses consist of a static part P_H and a dynamic part P_W which is caused by eddy currents. To assess soft magnetic materials concerning their eddy current related losses, it is necessary to have a model to describe, predict and explain the frequency dependence of the dynamic losses. This model needs to be easy and fast applicable. Such a model was developed by Bertotti using a simple loss separation ansatz. It contains the classical eddy current losses P_{cl} which can be explained by the electrical resistance and the excess eddy current losses P_{exc} which contain the domain wall movement.

This model has been used in this work to analyze a selection of soft magnetic materials. The dynamic coefficients have been calculated semi-analytical and compared to the coefficients gained from the simple loss separation ansatz fitting procedure.

Abstrakt

Weichmagnetische Materialien sind weitverbreitete und wichtige Werkstoffe in modernen Netzen zur Verteilung elektrischer Energie. Sie werden zum Beispiel als Kerne von Transformatoren und Generatoren verwendet, deren Wirkungsgrad unter anderem dadurch eingeschränkt wird, dass Energie dazu aufgewandt werden muss, die Magnetisierung im Material zu ändern.

In der vorliegenden Arbeit wurde die Frequenzabhängigkeit der Hystereseschleife an verschiedenen Werkstoffen (Fe-Si, nanokristallines Material etc.) untersucht. Die Messungen wurden mit einem selbstentwickelten Hysteresographen an ringförmigen Proben durchgeführt. Wesentlich bei derartigen Messungen ist die Form des angelegten Felds $H(t)$ oder $B(t)$. Eines der Ziele der hier vorliegenden Untersuchungen war den Effekt der Form von $H(t)$ bzw. $B(t)$ zu untersuchen. Es wurde ein sinusförmiges $H(t)$, ein dreieckförmiges $H(t)$ bzw. ein dreieckförmiges $B(t)$ verwendet und die so gemessenen Hysterese und deren Frequenzverhalten verglichen. Daraus kann dann durch Integration die Frequenzabhängigkeit der Verluste bestimmt werden.

Diese Ummagnetisierungsverluste setzen sich aus einem statischen Teil P_H und einem dynamischen Teil P_W zusammen, der durch Wirbelströme verursacht wird. Um weichmagnetische Materialien hinsichtlich ihrer wirbelstromabhängigen Verluste beurteilen zu können, ist es erforderlich ein Modell zu haben, das einfach und schnell anwendbar ist und die Frequenzabhängigkeit der dynamischen Verluste erfasst und erklärt. Ein solches Modell wurde von Bertotti mittels eines einfachen Verlustseparationsansatzes entwickelt. Es enthält die klassischen Wirbelstromverluste P_{cl} , die nur aus dem elektrischen Widerstand erklärt werden, und die anormalen Wirbelstromverluste P_{exc} die den Effekt der dynamischen Domänenwandbewegung enthält.

Dieses Modell wird in dieser Arbeit zur Analyse der Frequenzabhängigkeit der Verluste diverser weichmagnetischer Materialien verwendet. Die dynamischen Koeffizienten werden auch halb analytisch berechnet und mit den gefitteten Parametern verglichen.

Acknowledgement

I was fortunate enough to have been supported by so many and so much throughout my years of studying physics in every way possible and they all deserve my most heartfelt “Thank you!”.

First and foremost I want to express my sincerest gratitude to my very patient advisor Dr. Roland Größinger for his guidance and support throughout the work on this thesis by both giving me freedom and pushing me whenever needed. Also I want to thank Dr. Reiko Sato-Turtelli for many valuable discussions and her constant encouragement.

My gratitude also goes to Dr. Peter Mohn and Dr. Franz Keplinger who kindly agreed to be my examiners.

Of course there are many colleagues and friends who need to be thanked for their support. I am thankful to my office roommates Nasir Mehboob, Muhammad Atif, Stephan Sorta, Stefan Hartl and Cristina Grijalva as well as my colleagues from the neighbour offices. In no particular order I like to express my gratitude also to Martin Kriegisch, Thomas Huber, Bernhard Bergmair, Wolfgang Wallisch, Ahmad Asali, Peter Toson, Gregor Zickler and Patrick Heinrich. Thank you for making my time here easy and so enjoyable.

Also the personnel of the institute of solid state physics have been very supportive. Peter Hundegger, Markus Barcynski and Markus Schönhart have been very welcoming and supportive throughout my time here and cannot be forgotten when saying thank you.

Last but not least, I need to thank my family for supporting me in every way. My parents Agnes and Franz and my brother Franz have my heartfelt gratitude. Among my many aunts Anna Berthold has my sincerest gratitude for her financial support in particular and for keeping up with me in general. And of course I saved the most important thank you of all for last: It goes to Martina for being the most awesome sister possible.

Contents

Abstract.....	i
Abstrakt.....	ii
Acknowledgement.....	iii
Contents.....	iv
1. Introduction.....	1
1.1 Motivation.....	1
1.2 Magnetism: Properties and measurement basics.....	4
1.2.1 Properties, quantities and laws.....	4
1.2.1.1 Magnetic field strength H	4
1.2.1.2 Current linkage Θ	5
1.2.1.3 Magnetic flux Φ and magnetic flux density B	6
1.2.1.4 Permeability μ	7
1.2.1.5 Inductivity L	7
1.2.2 Magnetic materials and their properties.....	8
1.2.2.1 Hysteresis loops.....	8
1.2.2.2 Material classifications.....	11
1.2.3 Measurement principles.....	13
1.2.3.1 The ring sample.....	13
1.3 Losses.....	15
2. Methodology.....	20
2.1 Hardware.....	20
2.1.1 General Setup.....	20
2.1.2 KEPCO BOP 100 4-M.....	22
2.1.2.1 Operating range estimations.....	22
2.1.3 NI PCI 6120.....	28

2.2	Software	30
2.2.1	LabVIEW	30
2.2.2	C++	31
3.	Results	33
3.1	Hysteresis measurements on Fe ₇₅ Al ₂₅	33
3.1.1	Hysteresis for triangular H-field.....	33
3.1.2	Hysteresis for triangular B-field	34
3.2	Hysteresis measurements on Fe ₉₇ Si ₃	36
3.2.1	Hysteresis for triangular H-field.....	36
3.2.2	Hysteresis for sinusoidal H-field	37
3.2.3	Hysteresis for triangular B-field	38
3.3	Hysteresis measurements on Fe _{57,3} Ni ₁₀ Si _{33,3}	40
3.3.1	Hysteresis for triangular H-field.....	41
3.3.2	Hysteresis for sinusoidal H-field	42
3.3.3	Hysteresis for triangular B-field	43
3.4	Hysteresis measurements on VP 800-2	45
3.4.1	Hysteresis for triangular H-field.....	45
3.4.2	Hysteresis for triangular B-field	47
4.	Interpretation	49
4.1	Signal shapes and convergence speed.....	50
4.2	Permeability and inductivity	53
4.3	Validation of the loss model	57
5.	Summary.....	69
6.	Literature	71
	Appendices:	74
	Appendix A: Sample characteristics:.....	74

Appendix B: HysteresisMeasurements.vi: A short user manual.....	75
Appendix C: Mathematics of the model comparison process.....	79

1. Introduction

1.1 Motivation

Electromagnetic circuits or devices consist of resistors, capacitors, inductivities or even transformers. Transformers are used to transform AC-currents or AC-voltages. In order to do this with a high degree of efficiency soft magnetic cores play an important role. Fig. 1 shows the basic circuit of a simple transformer.

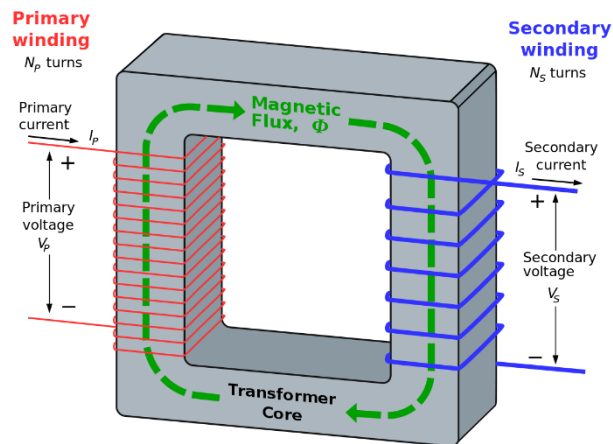


FIG. 1: BASIC SETUP OF A POWER TRANSFORMER [1]

Here the magnetic properties of the soft magnetic cores determine essentially the quality of such a transformer. A good soft magnetic core material should exhibit the following properties: high saturation magnetization, low coercivity, high permeability, low losses and a sufficient high Curie temperature (above room temperature) for technical applications.

Within this work the hysteresis properties of various soft magnetic materials are investigated. Special emphasis is laid on the determination of the losses. Here a fundamental question is how the hysteresis loop is measured applying an AC-field. Various possibilities exist concerning $H(t)$ or $B(t)$. It is the target of this work to find out under which condition the theoretically best understandable results can be achieved.

Fundamentals of theory

The transformer is an important element in a system that distributes electrical energy, enabling it at all to do so over far distances. It is essentially based on Faraday's law of induction

$$\vec{\nabla} \times \vec{E}(\vec{r}, t) = -\partial_t \vec{B}(\vec{r}, t)$$

EQ. 1

which is also the last of the four Maxwell's equations. These are

$$\begin{aligned}\vec{\nabla} \cdot \vec{D}(\vec{r}, t) &= 4\pi\rho(\vec{r}, t) & (a) \\ \vec{\nabla} \cdot \vec{B}(\vec{r}, t) &= 0 & (b) \\ \vec{\nabla} \times \vec{H}(\vec{r}, t) &= \frac{4\pi}{c}\vec{j}(\vec{r}, t) + \frac{1}{c}\partial_t \vec{D}(\vec{r}, t) & (c) \\ \vec{\nabla} \times \vec{E}(\vec{r}, t) &= -\frac{1}{c}\partial_t \vec{B}(\vec{r}, t) & (d)\end{aligned}$$

EQ. 2

and together with the constitutive relations

$$\begin{aligned}\vec{D} &= \varepsilon\vec{E} = \vec{E} + 4\pi\vec{P} & (a) \\ \vec{B} &= \mu\vec{H} = \vec{H} + 4\pi\vec{M} & (b) \\ \vec{j} &= \sigma\vec{E} & (c)\end{aligned}$$

EQ. 3

they describe the behaviour of electromagnetic fields in a solid state body.

Formally correct the equations 3.a to 3.d are called the phenomenological Maxwell's equations and are given in the cgs unit system, just like 4.a and 4.b.

While the cgs system has its advantages in some areas, the international SI unit system was used in this work.

The Maxwell's equations and constitutive relations in the SI system are:

$$\begin{aligned}\vec{\nabla} \cdot \vec{D}(\vec{r}, t) &= \rho(\vec{r}, t) & (a) \\ \vec{\nabla} \cdot \vec{B}(\vec{r}, t) &= 0 & (b) \\ \vec{\nabla} \times \vec{H}(\vec{r}, t) &= \vec{j}(\vec{r}, t) + \partial_t \vec{D}(\vec{r}, t) & (c) \\ \vec{\nabla} \times \vec{E}(\vec{r}, t) &= -\partial_t \vec{B}(\vec{r}, t) & (d) \\ \vec{D} &= \varepsilon\vec{E} = \varepsilon_0\vec{E} + \vec{P} & (e) \\ \vec{B} &= \mu\vec{H} = \mu_0(\vec{H} + \vec{M}) & (f)\end{aligned}$$

EQ. 4

In the equations above, E is the electric field strength caused by the charge ρ . The electric flux density D is not only contributed by E but also by a polarization term P (see Eq. 4.a) caused by a dielectric medium. E and D are connected via the dielectric constant ϵ , which is also called permittivity and consists of a relative part ϵ_r and a vacuum part ϵ_0 .

The magnetic field strength H and the magnetic flux density B are connected via the permeability μ . \vec{j} is the electric flux which is connected to the electric field E via the conductivity σ in Ohm's law (Eq. 4.c).

One always has to bear in mind, that the quantities in two different unit systems are not necessarily equal to one another but may be related by linear conversion factors as is the case with the cgs system and the SI system. These conversion factors can be looked up in any reputable set of lecture notes concerning electrodynamics [2]. To omit confusion, from now on, the SI system will be the only one used in this thesis.

To conclude the motivation for this work, Faraday's law of induction may once again be revisited for a closer look: The eddy current density is proportional to $\partial B/\partial t$. Later it is seen, that the hysteresis area is also partially proportional to losses due to eddy currents. While it is extremely common and easy to control the amplitude and shape of the H -field and thusly $\partial H/\partial t$, it would be very intriguing to examine, what the frequency behaviour of the losses is, if you control amplitude and shape of the B -field. For the course of this work, constant $\partial B/\partial t$ (triangular B -field) was chosen.

1.2 Magnetism: Properties and measurement basics

This chapter serves as an introduction to basic magnetism formulas and how different materials interact with a magnetic field as well as it also provides some theoretical background on measurement principles surrounding ring shaped samples.

1.2.1 Properties, quantities and laws

Before one can go deeper into the topic of losses, some basic magnetism formulas have to be introduced.

1.2.1.1 Magnetic field strength H

The magnetic field strength is a vector quantity which points in the direction of the tangent line to the field line. The magnitude of H is a measure for the strength of the field at that location.

Magnetic field strength outside a straight wire

$$H = \frac{I}{l} = \frac{I}{2\pi r}$$

EQ. 5

H is the magnetic field strength in $[A/m]$ which is given by the ratio of the current I in $[A]$ flowing through the wire and the length of the field line l in $[m]$ which can be calculated from the distance to the wire centre r by multiplying it with 2π . Naturally if you want to calculate the field outside a wire, this distance needs to be greater or equal than the mean wire radius, in short: $r \geq r_a$.

Magnetic field strength in the middle of a wire loop

$$H = \frac{I}{d} = \frac{I}{2r}$$

EQ. 6

The magnetic field strength H in $[A/m]$ in the middle of a wire loop is given by the ratio of the current I in $[A]$ and the mean diameter d in $[m]$ of the

wire loop which can naturally be written as $2 \cdot r$ with r being the mean radius of the wire loop in [m].

Naturally if you bend a wire of finite thickness the mean radius of the loop r needs to be bigger than the mean radius of the wire r_a , in short $r \geq r_a$.

Magnetic field strength inside a ring coil

$$H = \frac{I \cdot N}{l} = \frac{I \cdot N}{D \cdot \pi}$$

EQ. 7

The magnetic field strength H in [A/m] inside a ring coil is given by the ratio of the current I in [A] times the number of windings N and the mean magnetic path length l in [m] which can naturally be written as $D \cdot \pi$ where D in [m] is the mean diameter of the wire loop.

Naturally there are some boundary conditions to this formula also: the ring coil core needs to have a "thin" wall compared to its diameter, in short $D > 5 \cdot d$ with d being the wall thickness of the core in [m][3].

1.2.1.2 Current linkage Θ

$$\Theta = N \cdot I$$

EQ. 8

The current linkage Θ in [A] of a coil is given by the winding number N times the current I in [A] flowing through the coil. It represents the sum of all currents penetrating an area with an oriented border.

If Eq. 8 is inserted in Eq. 9, the result is Ampere's circuital law:

$$\Theta = N \cdot I = H \cdot l$$

EQ. 9

1.2.1.3 Magnetic flux Φ and magnetic flux density B

$$B = \frac{\Phi}{A}$$

EQ. 10

The magnetic flux density in $[T]$ is the ratio of the magnetic flux Φ in $[Wb]$ and the penetrated area A in $[m^2]$. The flux Φ is a scalar quantity and can be seen as the total number of magnetic B -field lines penetrating an oriented surface.

The important thing about the magnetic flux is, that it makes the B -field measurable

$$\frac{d}{dt}\Phi(t) = -U(t)$$

EQ. 11

because the time-derivative of Φ is proportional to the voltage induced in one coil turn.

Two important derived quantities from B and H are M and J . They can be calculated via one of the constituent laws

$$\vec{B} = \mu\vec{H} = \mu_0\vec{H} + \underbrace{\mu_0\vec{M}}_{\vec{J}}$$

EQ. 12

which can be rewritten to

$$\vec{B} = \mu_0(\vec{H} + \vec{M}) = \mu_0(1 + \chi_m)\vec{H}$$

EQ. 13

where χ_m is called the magnetic susceptibility.

For soft magnetic materials, one finds that $\vec{B} \approx \vec{J}$ often holds, because $\mu_0\vec{H}$ can be safely neglected for the involved H -fields [4]. What defines a soft magnetic material will be explained in 1.2.2 Magnetic materials and their properties.

1.2.1.4 Permeability μ

$$B = \mu \cdot H$$

EQ. 14

The magnetic flux density B in $[T]$ is the permeability μ in $[(V \cdot s)/(A \cdot m)]$ times the magnetic field strength H . The permeability μ consists of a relative part μ_r and a vacuum part μ_0 .

The vacuum permeability has the value:

$$\mu_0 = 4 \cdot \pi \cdot 10^{-7} \left[\frac{V \cdot s}{A \cdot m} \right]$$

EQ. 15

The relative permeability μ_r will be further explained in 1.2.2 Magnetic materials and their properties, as it poses an excellent opportunity to sort magnetic materials in different categories.

1.2.1.5 Inductivity L

$$\Phi = L \cdot I$$

EQ. 16

The inductivity of one single wire turn L in $[H]$ is the proportionality factor of the current I in $[A]$ to calculate the magnetic flux Φ in $[Wb]$.

Thusly the inductivity of a coil is the number of turns N times the ratio of the magnetic flux Φ and the current I .

$$L = N \frac{\Phi}{I} = \frac{\mu AN^2}{l}$$

EQ. 17

Φ/I can be replaced by inserting the equations 8 and 14. For a ring coil, l is calculated as follows:

$$l_{ring} = d_m \cdot \pi$$

EQ. 18

l is also called the mean magnetic path length while d_m is the mean diameter of the ring core.

1.2.2 Magnetic materials and their properties

As mentioned before, the relative permeability μ_r can be used to classify magnetic materials. Depending on the value of μ_r , they are called diamagnetic, paramagnetic, ferromagnetic or ferrimagnetic materials. In the case of magnetic metals which are important for this work, one is only concerned with the strongest of these five ordering types namely, ferromagnetism [5].

Probably the most distinctive feature of ferromagnetism is the existence of a hysteresis loop caused by domains and consequently μ_r depending on the H -field in a very complex manner.

The different types, their parts and shapes of hysteresis will be explained in the next section.

1.2.2.1 Hysteresis loops

Types of hysteresis loops

The two most common ways to plot a hysteresis are shown by the pictures below:

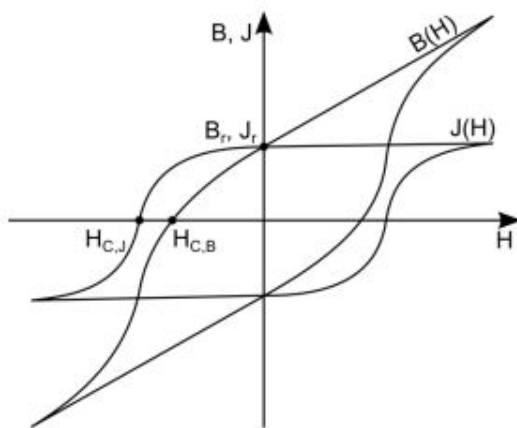


FIG. 2: HYSTERESIS LOOPS AS B(H) AND J(H) CURVES [6]

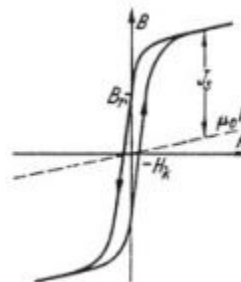


FIG. 3: CONTRIBUTION OF J TO THE MAGNETIC FIELD B [7]

Either B or J are plotted versus the magnetizing field H . J is most intriguing from a mere theoretical solid state physicists point of view because of J being a measure of the spins alignment in the direction of the H -field. B is most intriguing from a practical electrotechnicians point of view, because it can be directly measured, also the area of the $B(H)$ -loop is proportional to the losses in the core material as will be explained later. As illustrated by [7] in Fig. 3, J represents the contribution of the material itself to the hysteresis loop.

The magnetization process

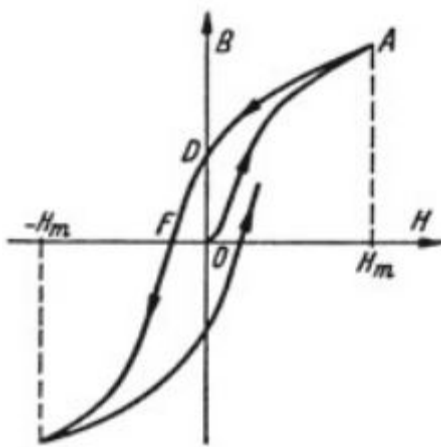


FIG. 4: CHARACTERISTIC POINTS IN THE HYSTERESIS LOOP DURING A MAGNETISATION CYCLE STARTING FROM A COMPLETELY DEMAGNETISED STATE [7]

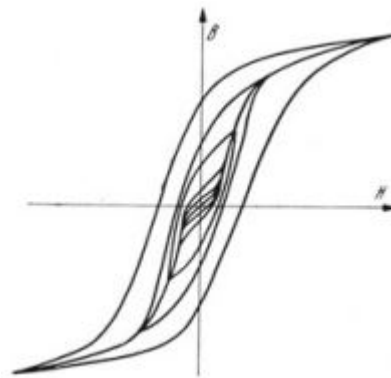


FIG. 5: THE COMMUTATION CURVE AS LOCUS OF THE MINOR LOOPS [7]

If a material is completely demagnetized and a periodical magnetizing field H is applied, the flux density B follows the initial magnetization curve from the origin “O” to the point “A” where the maximum H -field is achieved. When reducing the H -field now, the B -field does not decrease as steep as the virgin curve increased and so, when H arrives at zero (point “D”), a remanent flux density B_r is still present. When the H -field is decreased further so that the flux density is zero, the coercive field H_c determines this point where B becomes zero (point “F”). Increasing the absolute value of the H -field from this point on leads to B going there to the (negative saturation and then decreasing the field the (negative) remanent point B_r is reached ($H = 0$). Increasing then H delivers the (positive)

coercive point ($B = 0$) and finally reaching the (positive) saturation closes the hysteresis. A “well” measured hysteresis loop has to be a closed curve where positive and negative B_r and positive and negative H_c has to be equal.

Traditionally, only the so called “outermost hysteresis” is called hysteresis, while the inner hystereses are called minor loops. The initial magnetization curve of the outermost hysteresis is called virgin curve. Another characteristic line for a material is given by connecting the reversal points of the minor loops recorded with time dependent H -fields of constant frequency and increasing amplitude. It is called the commutation curve. If the amplitudes of H are smaller than H_c of the outermost hysteresis, the commutation curve does not differ very much from the virgin curve. If the amplitudes are significantly larger than this H_c it is easy to see that the commutation curve is flatter than the virgin curve of the outermost hysteresis.

The demagnetization process

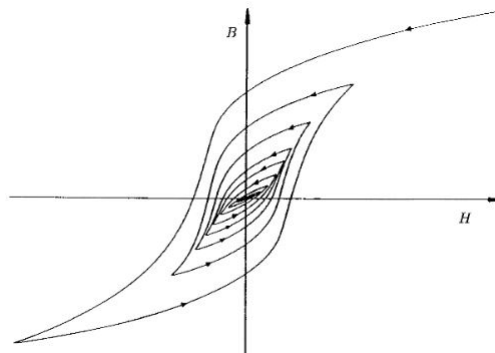


FIG. 6: HYSTERETISIS TYPE CURVES IN THE DEMAGNETISATION PROCESS [8]

It is always important when performing a hysteresis measurement to have repeatable measurement conditions. If a magnetization curve is started without a demagnetization procedure performed first, the initial curve will not start at the origin but somewhere between the negative and positive value of B_r . So it is evident, that a sample must be demagnetized before a measurement is started.

One of the possibilities of demagnetizing a sample is very simple:

A periodic H -field is applied and the amplitude is decreased (exponentially) for a certain time. The demagnetization procedure used in this thesis was a damped sine-

shaped H -field starting with the maximum amplifier output and a frequency of 1 Hz . The damping was exponential with a time-constant of two seconds. The whole process lasts 15 seconds and was enough for all samples used to start their virgin curves in the low two-digit- $[mT]$ range around the origin.

As a rule of thumb, one can say that the following steps benefit the demagnetization quality

- Increase of the starting amplitude of the periodic signal.
- Decrease of the frequency of the periodic signal.
- Increase of the damping constant so that the signal decreases slower in combination with a longer demagnetization duration.

Depending on the sample properties, the measurements can be performed applying a non-sinusoidal H -field, for example a triangular H -field. Also the damping does not need to be exponential but can also be linear. The above described procedure however worked best for the selection of samples used during this work.

1.2.2.2 Material classifications

As the topic of this thesis is losses in soft magnetic materials, one needs to define what “soft” means when talking about magnetism.

Hard and soft magnetic materials

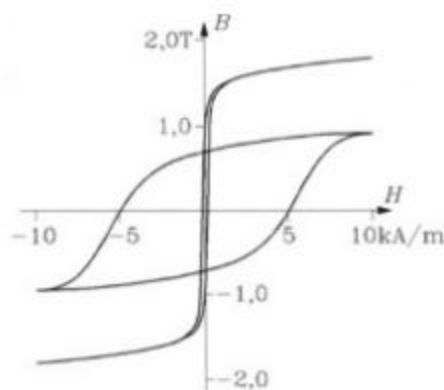


FIG. 7: TYPICAL HYSTERESIS OF SOFT AND HARD MAGNETIC MATERIAL [3]

Fig. 7 shows a typical soft magnetic hysteresis which is very narrow and has a high flux density while a hard magnetic hysteresis in contrary to that has a

very high coercive field. A soft magnetic material is easy to magnetize and suitable for transformer and shielding applications while a hard magnetic material needs higher fields to be magnetized and is suitable for applications where permanent magnetic properties are needed. The narrow curve in Fig. 7 shows a hysteresis of an iron silicon alloy while the wide curve is a hysteresis of steel with 1 % carbon.

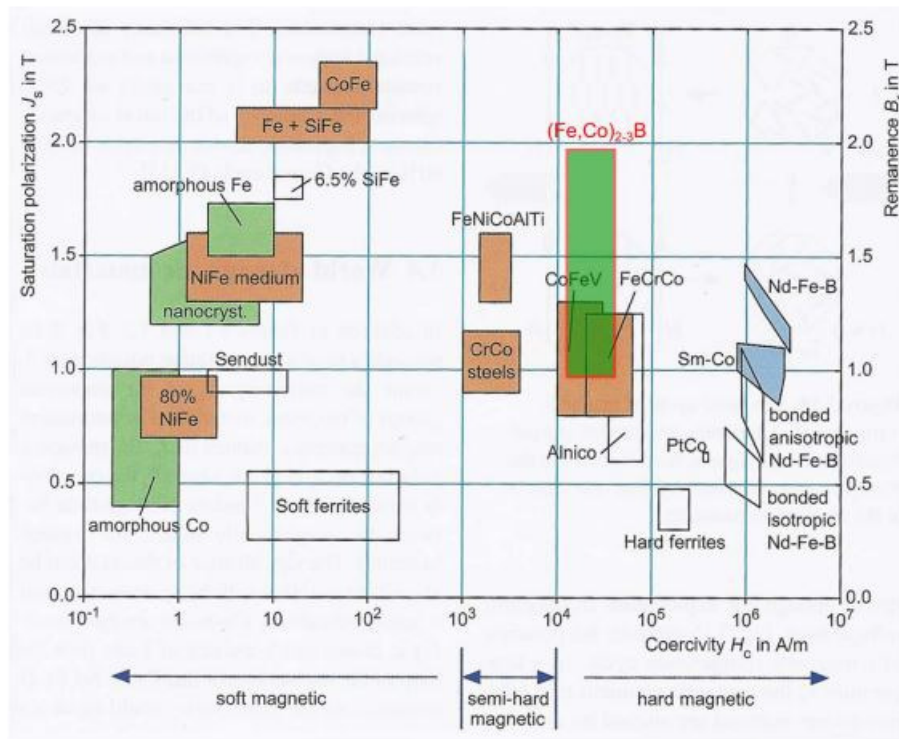


FIG. 8: IMPORTANT GROUPS OF MAGNETIC MATERIALS ACCORDING TO [5] AND [6]

Fig. 8 shows magnetic alloys that can be used for various applications in technique. Generally speaking, one can consider any material with a H_c value of $1 [kA/m]$ and smaller as soft and up to $10 [kA/m]$ semi-hard magnetic. Materials with a H_c value greater than $10 [kA/m]$ are considered hard magnetic. In the next chapter (1.2.3) it will be explained, why it makes sense to measure only soft magnetic materials as ring shaped samples while hard magnetic materials are generally investigated in a magnetic open system.

1.2.3 Measurement principles

Before we can go in medias res with the losses, let us summarize the important facts about the measurement principles

1.2.3.1 The ring sample

Generally magnetic measurements are performed on many different shapes depending on the material and on the set-up used. For soft magnetic materials the demagnetizing field changes the shape of the loop essentially because it is generally much higher than the applied field (see Eq. 19). Therefore it is favourable to measure the hysteresis loop in a magnetically closed arrangement. Typical examples are here ring shaped or frame shaped samples.

Beside these more fundamental considerations one uses ring shaped samples for loss measurements because the standard for measuring power losses and amplitude permeability tells to do so [9]. There are several good reasons for using this geometry: If one wants to measure the amplitude permeability and the power losses (as in this work) the core has to be ring shaped (while the ratio of outer to inner diameter may not be greater than 1.4) and the windings need to be as close as possible to the core and equally distributed around the circumference for only then is the coupling factor as close to one as possible. Additionally “air-coil” contributions are neglectable.

Also, one has to keep in mind, that according to the second Maxwell’s equation (Eq. 2 and Eq. 4 b) there can be no magnetic monopoles and the magnetic field lines must thusly be closed. Geometries which do not fulfil this condition cause the external field H_{ext} not to penetrate the magnetic material entirely. This is described by the following equation

$$H_{int} = H_{ext} - N \cdot M(H)$$

EQ. 19

where N is the so called demagnetizing factor ($0 < N \leq 1$) describing this problem. N depends on the geometry of the sample and can only be calculated exactly for very few geometries, among them the ring, where N is zero because all the field

lines are closed in a ring (assuming a high permeability). This means, that the applied external field of the coil is exactly the field inside the core.

The basic formulas that one needs to calculate the field within ring samples are:

$$H = \frac{I \cdot N_1}{l_m}$$

EQ. 20

EQ. 21: MAGNETIZING FIELD H IN $[A/m]$, DEPENDING ON THE CURRENT I THROUGH THE PRIMARY COIL, THE NUMBER OF PRIMARY WINDINGS N_1 AND THE MEAN MAGNETIC PATH LENGTH l_m

$$B = \frac{1}{N_2 \cdot A_{Fe}} \int U_2(t) dt$$

EQ. 22

EQ. 23: MAGNETIC FLUX DENSITY B , DEPENDING ON THE NUMBER OF SECONDARY WINDINGS N_2 , THE EFFECTIVE IRON-CROSS SECTION A_{Fe} AND THE INTEGRAL OF THE VOLTAGE U_2 INDUCED IN THE SECONDARY WINDING

$$A_{Fe} = A \cdot k_{Fe}$$

EQ. 24

EQ. 25: EFFECTIVE IRON CROSS SECTION A_{Fe} , DEPENDING ON THE GEOMETRICAL CROSSSECTION A OF THE SAMPLE AND THE LAMINATION NUMBER k_{Fe} WHICH IS ONE FOR BULK SAMPLES AND DENOTES THE PERCENTAGE OF THE FE-CROSSSECTION TAKEN UP BY MATERIAL WHICH IS GLUED FROM THIN PLATES OR FOR AIR LAMINATED SAMPLES

$$l_m = \frac{d_a + d_i}{2} \pi$$

EQ. 26

EQ. 27: THE MEAN MAGNETIC PATH LENGTH l_m , DEPENDING ON THE OUTER AND INNER DIAMETER OF THE SAMPLE d_a AND d_i

$$A = d_w \cdot h$$

EQ. 28

EQ. 29: GEOMETRICAL CROSS SECTION A , DEPENDING ON THE WALL THICKNESS d_w AND THE SAMPLE HEIGHT h

One uncertainty is here the calculation of the magnetic path length l_m . Eq. 26 assumes a constant permeability as well as a constant field H over the cross section of the ring. Therefore the difference between d_a and d_i should be as small as possible ($d_a/d_i \leq 1.4$).

1.3 Losses

This chapter shall be a recap of what Bertotti [4] has to say about the losses in ferromagnetic materials and their frequency behaviour. Later it shall be examined if and for what material and signal conditions the simple separation ansatz with hindsight to their cause hold true.

$$\frac{P}{f} = \int_{loop} H_a dB$$

EQ. 30

represents the energy per unit volume transferred to the thermal bath in one magnetization cycle. P is the power loss and $\frac{P}{f}$ the loss per cycle. The loss per cycle consists of a static part P_H called "hysteresis loss" and a dynamic part P_W depending on eddy current effects [5].

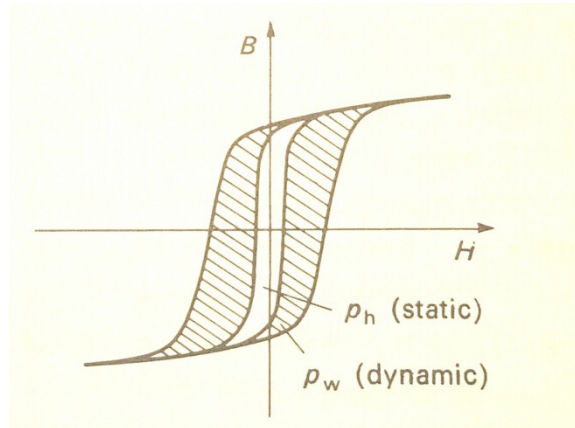


FIG. 9: COMPOSITION OF THE LOSSES FROM A STATIC PART P_H AND AN EDDY CURRENT DEPENDENT PART P_W ACCORDING TO [5]

If the space time distribution $\vec{j}(\vec{r}, t)$ of the eddy current density would be completely known and the eddy currents are the main contributor for the losses, then the loss per cycle could be calculated as follows:

$$\frac{P}{f} = \int_V \frac{1}{V} d^3r \int_0^{1/f} \frac{|\vec{j}(\vec{r}, t)|^2}{\sigma} dt$$

EQ. 31

The losses per cycle depending solely on the eddy currents consist of an integral of the eddy current density over one cycle over the sample volume. It also depends on the electric conductivity σ of the soft magnetic material. The volume integral part

$$\int_V \frac{1}{V} d^3r$$

EQ. 32

can be reduced according to [10] for geometrical considerations to

$$\int_A \frac{1}{A} d^2r$$

EQ. 33

which poses an integral over the sample cross section A. This reduces Eq. 31 to

$$\frac{P}{f} = \int_A \frac{1}{A} d^2r \int_0^{1/f} \frac{|\vec{j}(\vec{r}, t)|^2}{\sigma} dt$$

EQ. 34

One also often finds that the frequency behaviour of the losses per cycle is not far from

$$\frac{P}{f} = C_0 + C_1 \cdot f + C_2 \cdot \sqrt{f}$$

EQ. 35

where C_0 represents P_H and C_1 together with C_2 represents P_W . An exemplary plot for a loss separation like this can be seen below:

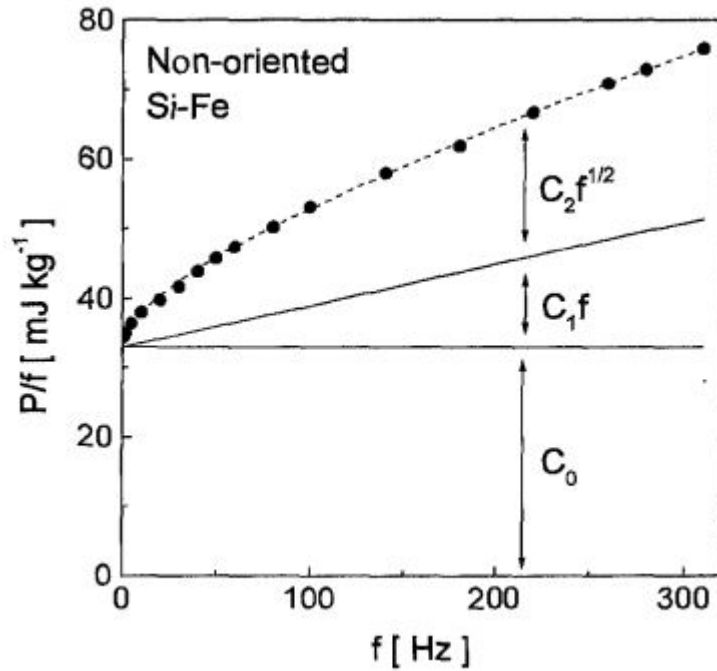


FIG. 10: EXAMPLE FOR SEPARATION OF THE LOSSES ACCORDING TO [4]

Bertotti mentions, that it is remarkable for such an equation to exist at all if you consider the complex mechanisms involved in the magnetization process and then again not because most of the time very few mechanisms are dominant.

Generally speaking, the losses can be separated in three different parts:

- Hysteresis losses
- Classical eddy current losses
- Excess eddy current losses

where the hysteresis losses are the static part P_H and the sum of the latter two is the dynamic part P_W . The loss per cycle P/f can be rewritten to

$$P = P_{hyst} + P_{cl} + P_{exc}$$

EQ. 36

by multiplying it with f .

If one wants to investigate the classical and the excess eddy current losses, Bertotti also provides a formula directly derived from the Maxwell's equations:

$$P(t) = P_{hyst}(t) + \frac{\sigma d^2}{12} \left(\frac{dJ}{dt} \right)^2 + \sqrt{\sigma G A V_0} \left| \frac{dJ}{dt} \right|^{\frac{3}{2}}$$

EQ. 37

where the individual terms correspond to those in Eq. 36. While the classical eddy current losses P_{cl} are proportional to the mean overall specific electric conductivity (via the electric conductivity σ and the slab thickness d), the excess eddy current losses P_{exc} are proportional to microstructure related parameters (G , A and V_0) factoring in the size and shape of the grains in addition to the conductivity σ .

This is possible because of the following reasons. The statistic distribution of the Barkhausen jumps is proportional to the magnetization rate dJ/dt . These elementary magnetization jumps correspond to the sudden and localized displacement of the domain walls [10]. As already mentioned in 1958 by Pry and Bean [11], the displacement of the domain walls is the origin of the dynamic losses.

The classical losses at constant magnetization dJ/dt rate according to [10] are:

$$P^{cl} \approx \frac{\sigma d^2}{12} \left(\frac{dJ}{dt} \right)^2 \left(1 - \frac{\sigma \mu d^2}{\pi^2} f \right)$$

EQ. 38

In case of Bertotti's low-frequency-limit approximation, the term proportional to f , which determines the shielding effects of eddy currents, can be neglected. This can be done so because the generated field of the eddy currents is much smaller than the applied field.

Bertotti also provides a formula for the classical losses $P_{cl}(t)$ to validate the loss separation formula more easily:

$$P_{cl}(t) = \frac{\sigma d^2}{12} \left(\frac{dB}{dt} \right)^2$$

EQ. 39

What is interesting about this formula is that one can calculate the time average over one cycle of the hysteresis. It can be reduced with $dB/dt = \pm 4B_{max}f$ for constant dB/dt to

$$P_{cl}^{TRI} = \frac{4}{3}\sigma d^2 B_{max}^2 f^2$$

EQ. 40

Comparing Eq. 35, the simple loss separation ansatz with Eq. 37, the formula for arbitrary excitation, the following associations can be made:

$$\begin{aligned} P_{hyst} &= C_0 \cdot f & (a) \\ P_{cl} &= \frac{\sigma d^2}{12} \left(\frac{dJ}{dt}\right)^2 = C_1 \cdot f^2 & (b) \\ P_{exc} &= \sqrt{\sigma GAV_0} \left|\frac{dJ}{dt}\right|^{\frac{3}{2}} = C_2 \cdot f^{\frac{3}{2}} & (c) \end{aligned}$$

EQ. 41

For whatever signal shape of $H(t)$ or $B(t)$ this holds to be true, aside from frequency behaviour of eddy current caused losses, it would also pose a potential method for calculating the conductivity σ solely from hysteresis measurements because d is simply the sample height.

2. Methodology

One of the methods to measure a hysteresis is the so called transformer method. A current $I(t)$ is applied to the primary winding and generates a magnetizing field with the strength $H(t)$ and induces a voltage in the secondary winding that is proportional to the time-derivative $\partial B/\partial t$ of the magnetic flux density $B(t)$. To get the flux density, the secondary voltage U_2 has to be integrated and scaled (see Chapter 1). One gets a hysteresis by plotting the B -field versus the H -field.

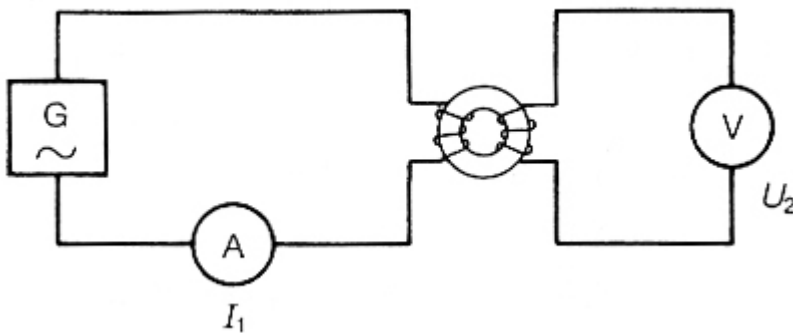


FIG. 11: SETUP OF THE TRANSFORMER METHOD TO MEASURE A HYSTERESIS [5]

2.1 Hardware

2.1.1 General Setup

The basic principle of the hysteresis set-up is very simple: a voltage $U_1(t)$ is generated on a PC via a measurement card and applied to a voltage controlled current source. The current $I(t)$ drives the primary side while being measured via the voltage drop on a shunt resistor. On the secondary side there is a voltage $U_2(t)$ measured which is proportional to the time derivative of the B -field.

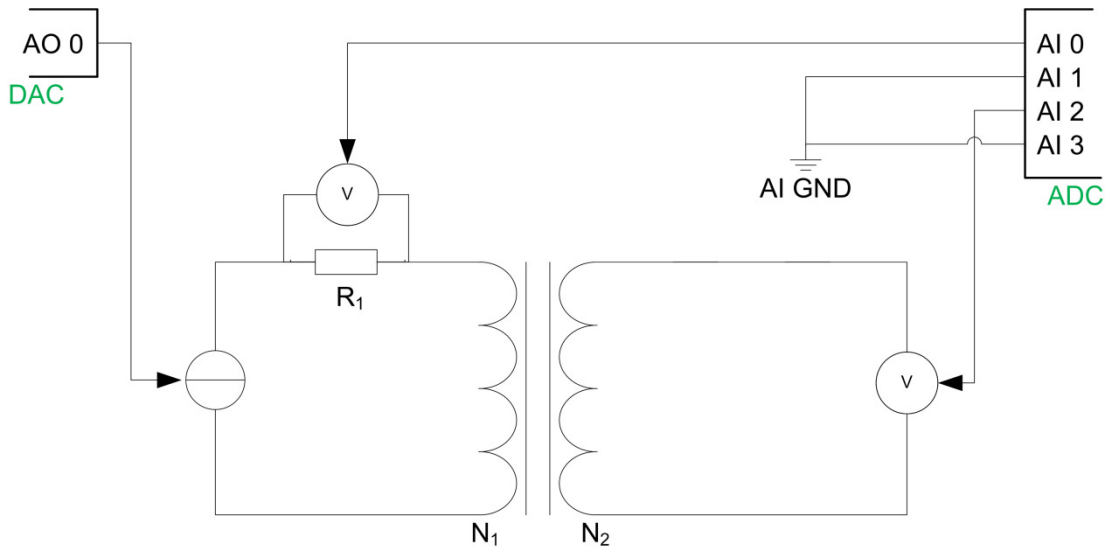


FIG. 12: SCHEMATIC OF THE MEASUREMENT-SETUP [12]

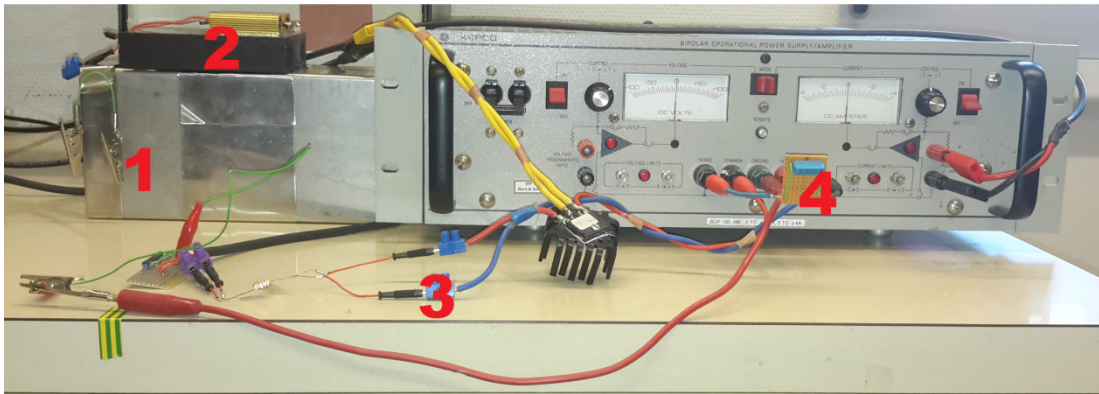


FIG. 13: PICTURE OF THE MEASUREMENT SETUP: 1 IS AN OPTIONAL MUMETALL BOX THAT THE SAMPLE CAN BE PUT IN AND THAT CAN BE GROUNDED VIA THE CLAMPS ON THE RED AND GREEN CABLE, 2 IS AN OPPTIONAL SERIES RESISTOR ON COOLING FINS THAT CAN BE MOUNTED AT POINT 3, 4 IS AN OPTIONAL COMPENSATION CAPACITOR FOR NOISE SENSITIVE MEASUREMENTS AND HIGH LOAD INDUCTIVITIES

To make the system as reliable as possible, it has to be considered, that there may be orders of magnitude between the voltage U_1 (proportional to the current I on the primary side) and the voltage U_2 (proportional to $\partial B/\partial t$). Such differences are faced best with a multichannel ADC (see 2.1.3.)

Nevertheless, like in [12], National Instruments' guidelines for working with a card with one ADC and a multiplexer switching between the channels of this card were considered to make the system as versatile as possible. This means, that measuring channels are not "neighbours", but are separated by channels connected to the

cards ground potential to omit ghosting in between channels caused by signals of vastly different magnitude. Also, to be prepared for measuring under so called floating ground conditions, the channel responsible for the secondary voltage measurement was connected to the sample via a voltage divider where the centre tap was also connected to the measurement cards ground potential.

2.1.2 KEPCO BOP 100 4-M

The power supply used in this thesis is a “KEPCO BOP 100-4M”, a 400 *Watt* bipolar power supply. When operated in current mode, it poses a rigid and frequency stable voltage controlled current source which is specially designed for driving inductive loads. The inductive loads may only be up to 0.5 *mH* without performance deterioration according to the manual. When working with loads of a higher inductivity, a compensation capacitor may be connected across the output pins. This capacitor can be in the range of 0.01 μF to 1 μF [13].

2.1.2.1 Operating range estimations

To investigate the limits of the amplifiers operating range, an equivalent circuit model of the operational amplifier and its load has to be created. This is necessary to get a better grasp of the BOP’s behaviour under inductive loads.

The equivalent circuit of a voltage controlled current source is well known:

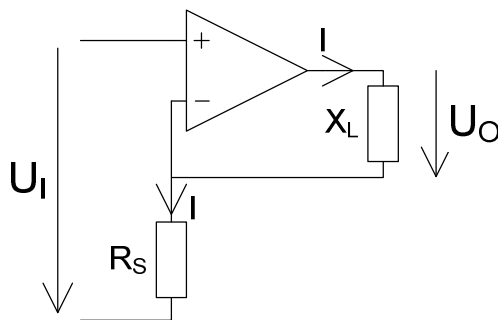


FIG. 14: EQUIVALENT CIRCUIT OF A VOLTAGE CONTROLLED CURRENT SOURCE DRIVING A LOAD OF ARBITRARY IMPEDANCE X_L

The current flowing through the load X_L is controlled via the voltage drop on the resistor R_s and does not depend on the load but on the value of R_s only. The load

in the above equivalent circuit is an arbitrary impedance, that can be modelled as follows:

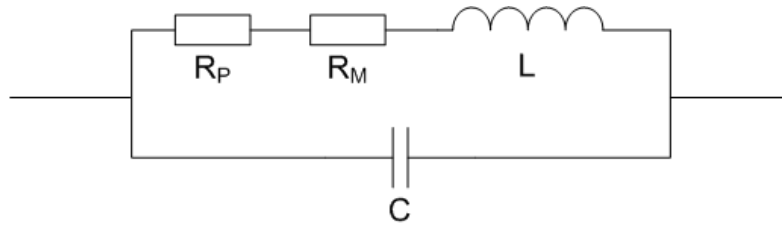


FIG. 15: EQUIVALENT CIRCUIT OF THE LOAD

L symbolizes the samples primary side inductivity while R_M stands for the resistance that causes a current proportional voltage drop, by which the actual electrical current flowing through the samples primary side can be measured. R_P and C pose a series resistor and a compensation capacitor which are needed to mitigate the effects of highly inductive loads. The electrical impedance of the load can be written as

$$X_L(j\omega) = [j\omega C + (R_P + R_M + j\omega L)^{-1}]^{-1} = \frac{R_P + R_M + j\omega L}{1 + j\omega C[R_P + R_M] + (j\omega)^2 LC}$$

EQ. 42

To investigate certain stability criteria for assessing the operating range limits of the amplifier, the equivalent circuit has to be redrawn so that the transfer function can be written down easily:

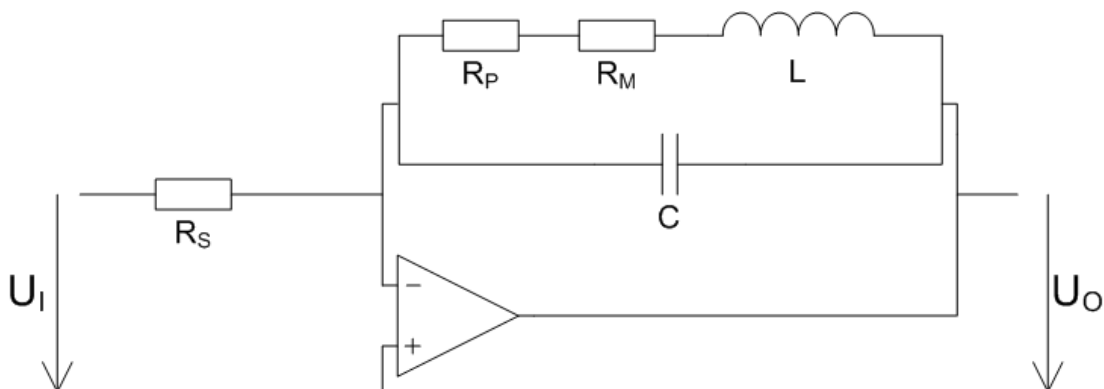


FIG. 16: EQUIVALENT CIRCUIT OF THE TOTAL MEASUREMENT SETUP

The Laplace transformation of the transfer function can now directly be written as follows:

$$G(s) = -\frac{R_P + R_M}{R_S} \frac{1 + s\frac{L}{R_P + R_M}}{1 + sC[R_P + R_M] + s^2LC}$$

EQ. 43

It can be associated with a series connection of a PD element and a PT2 element and poses a PDT2 element. The coefficients of s and frequency independent factor prior to the main fraction pose characteristic values of the transfer function which can be used to assess the stability in a suitable program like Matlab via analyzing the Bode plot and the frequency response.

Symbol	Value	Meaning
k	$-\frac{R_P + R_M}{R_S}$	Proportionality factor
T_D	$\frac{L}{R_P + R_M}$	Corner frequency of the PD-element
ω_n	$\sqrt{\frac{1}{LC}}$	Frequency of the undamped oscillation of the PT2 part
D	$C[R_P + R_M]\omega_n$	Damping factor of the PT2 part

TAB. 1: CHARACTERISTIC VALUES OF THE SYSTEMS TRANSFER FUNCTION

Desired behaviour according to [14] and [15] is achieved by increasing the damping parameter as high as possible, at least $D > 1/\sqrt{2}$ has to be achieved so that peaking in the frequency gain plot of the Bode plot is omitted.

A first attempt to achieve this was to increase the damping by varying the values of C according to [13] for different values of the loads inductivity. Eventually the damping was increased further by increasing the value of a resistor in series with the load. The values for C come directly from the manual of the amplifier; the values for R follow from empirical considerations.

TF-Nr	R_P	R_M	R_S	L	C	k	T_D	ω_n	D	
	[Ω]	[Ω]	[Ω]	[mH]	[μF]	[1]	[s]	[rad/s]	[1]	
f00	0	0.1	2.5	0	0	-0.04	0			
f01	22	0.1	2.5	0	0	-8.84	0			
f02	0	0.1	2.5	0.01	0	-0.04	0.1 m			
f03	0	0.1	2.5	0.02	0	-0.04	0.2 m			
f04	0	0.1	2.5	0.05	0	-0.04	0.5 m			
f05	0	0.1	2.5	0.1	0	-0.04	1 m			
f06	0	0.1	2.5	0.2	0	-0.04	2 m			
f07	0	0.1	2.5	0.5	0	-0.04	5 m			
f08	0	0.1	2.5	1	0	-0.04	10 m			
f09	0	0.1	2.5	0.1	0.01	-0.04	1 m	1000 k	0.5 m	
f10	0	0.1	2.5	0.2	0.01	-0.04	2 m	707 k	0.35 m	
f11	0	0.1	2.5	0.5	0.01	-0.04	5 m	447 k	0.22 m	
f12	0	0.1	2.5	1	0.01	-0.04	10 m	316 k	0.16 m	
f13	0	0.1	2.5	0.1	0.1	-0.04	1 m	316 k	1.6 m	
f14	0	0.1	2.5	0.2	0.1	-0.04	2 m	224 k	1.1 m	
f15	0	0.1	2.5	0.5	0.1	-0.04	5 m	141 k	0.7 m	
f16	0	0.1	2.5	1	0.1	-0.04	10 m	100 k	0.5 m	
f17	0	0.1	2.5	0.1	1	-0.04	1 m	100 k	5 m	*)
f18	0	0.1	2.5	0.2	1	-0.04	2 m	70.7 k	3.5 m	
f19	0	0.1	2.5	0.5	1	-0.04	5 m	44.7 k	2.2 m	
f20	5	0.1	2.5	1	1	-0.04	10 m	31.6 k	1.6 m	
f21	5	0.1	2.5	0.1	1	-2.04	19.6 μ	100 k	0.255	
f22	5	0.1	2.5	0.2	1	-2.04	39.2 μ	70.7 k	0.180	
f23	5	0.1	2.5	0.5	1	-2.04	98.0 μ	44.7 k	0.114	
f24	5	0.1	2.5	1	1	-2.04	196.1 μ	31.6 k	0.081	
f25	10	0.1	2.5	0.1	1	-4.04	9.9 μ	100 k	0.505	
f26	10	0.1	2.5	0.2	1	-4.04	19.8 μ	70.7 k	0.357	
f27	10	0.1	2.5	0.5	1	-4.04	49.5 μ	44.7 k	0.226	
f28	10	0.1	2.5	1	1	-4.04	99.0 μ	31.6 k	0.159	
f29	22	0.1	2.5	0.1	1	-8.84	4.52 μ	100 k	1.105	**)
f30	22	0.1	2.5	0.2	1	-8.84	9.05 μ	70.7 k	0.781	
f31	22	0.1	2.5	0.5	1	-8.84	22.6 μ	44.7 k	0.494	
f32	22	0.1	2.5	1	1	-8.84	45.2 μ	31.6 k	0.349	

TAB. 2: CHARACTERISTIC VALUES OF THE TRANSFER FUNCTION $G(j\omega)$ RESPECTIVELY OF THE TRANSFER FUNCTIONS LAPLACE TRANSFORM $G(s)$ FOR DIFFERENT LOAD AND COMPENSATION CONDITIONS

*) Unfortunately the maximum recommended compensation capacitor was not enough to get close to a desired value of the damping constant D .

***) A series resistor with the value of 22Ω gets the damping in the widest possible range of L to a stabilized or at least not resonant operation condition for the amplifier.

The values of D indicate the limits of L which the operational amplifier can tolerate without deterioration in the whole frequency range. This value is somewhere between $0.2 [mH]$ and $0.5 [mH]$ because in this range, neither peaking in the bode diagrams frequency gain plot should occur nor should the amplifier exceed his power range by being set to maximum gain¹.

This can be verified by examining the bode plot of the four most promising compensation setups (f29 to f32):

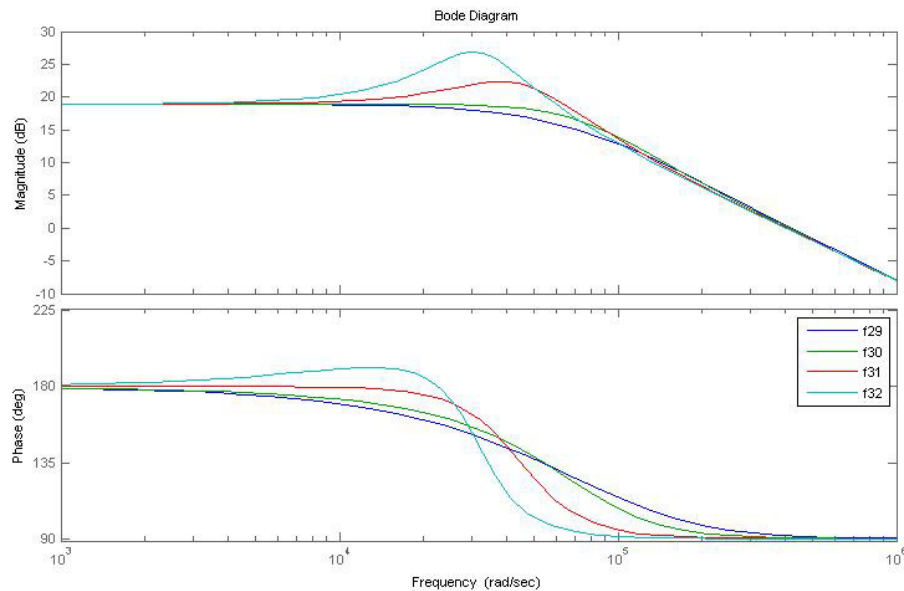


FIG. 17: BODE PLOT OF THE TRANSFER FUNCTIONS WITH MAXIMUM DAMPING FOR DIFFERENT INDUCTIVITIES

¹ Amplification of U_I by a gain of 10 means that the frequency gain would cross the 20 dB line.

To assess the behaviour of these setups not only in the image space but also in the time domain, the step response of the same four transfer functions is examined:

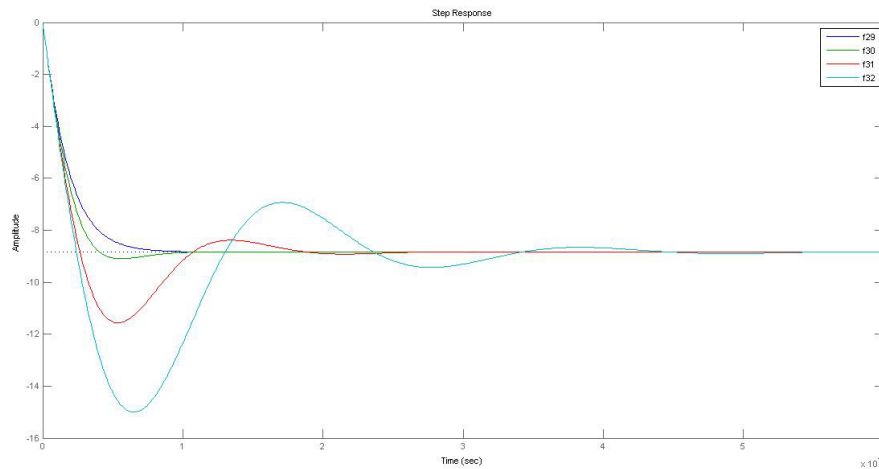


FIG. 18: STEP RESPONSE OF THE TRANSFER FUNCTIONS WITH MAXIMUM DAMPING FOR DIFFERENT INDUCTIVITIES

It can be seen easily in the bode plot, that the two transfer functions with a damping constant below $1/\sqrt{2}$ show peaking in the frequency gain plot while those with a damping constant larger than $1/\sqrt{2}$ show no peaking in the frequency gain plot at all. It is also clearly visible, that the two systems with the poorer damping would demand more than the maximum gain of 20 dB from the amplifier. This suggests that loads with inductivity in this order of magnitude may not be operated in the full frequency range but only up to a critical gain crossover frequency. Unfortunately it is not possible to exactly determine the value of this frequency for a real coil because of the inductivities non-trivial frequency dependence itself. This frequency dependence is caused by the permeability of the coil core, which in this case is the sample.

Thusly it follows, that for loads bigger than 0.2 [mH] this frequency may only be approached empirically by examining each measurement for signs of the maximum gain being set and the amplifiers power range being exceeded.

It is clearly visible in the step response plot, that the setups with the better damping show no or minimal overshooting.

2.1.3 NI PCI 6120

To process the voltage signals from and to the measurement system, a measurement card is needed. The measurement card used during this thesis was a NI PCI 6120 card from National Instruments that interacts with the measurement system via a BNC-connector box².

The card features a dedicated analogue-to-digital converter per channel which makes multichannel data acquisition much more fail-safe than on a card with one analogue-to-digital converter and a multiplexer to switch between those channels.

Also the ADC of this card has a 16 bit resolution on each analogue input channel, which has huge advantages over the very common 12 bit resolution. As one can see with [16], a system with an identical set-up, the noise of a system like the one used in this thesis has a $U_{Peak-Peak}$ -value in the range of 150 to 200 μV . Usually the lowest measurement range for these cards (highest resolution) has a scale-end-value of 0.2 V, which means, that the least significant bit (= measure for the resolution) is $\sim 98 \mu V$, which in turn means, that with a 12 bit card one cannot distinguish between a “bad” measurement and the systems inherent noise. A 16-bit system offers a resolution of $\sim 6 \mu V$ in the same measurement range, which is better by the factor $2^4 = 16$ than a 12 bit system. This is crucial here.

² The connector box used was the NI BNC 2110 connector box.

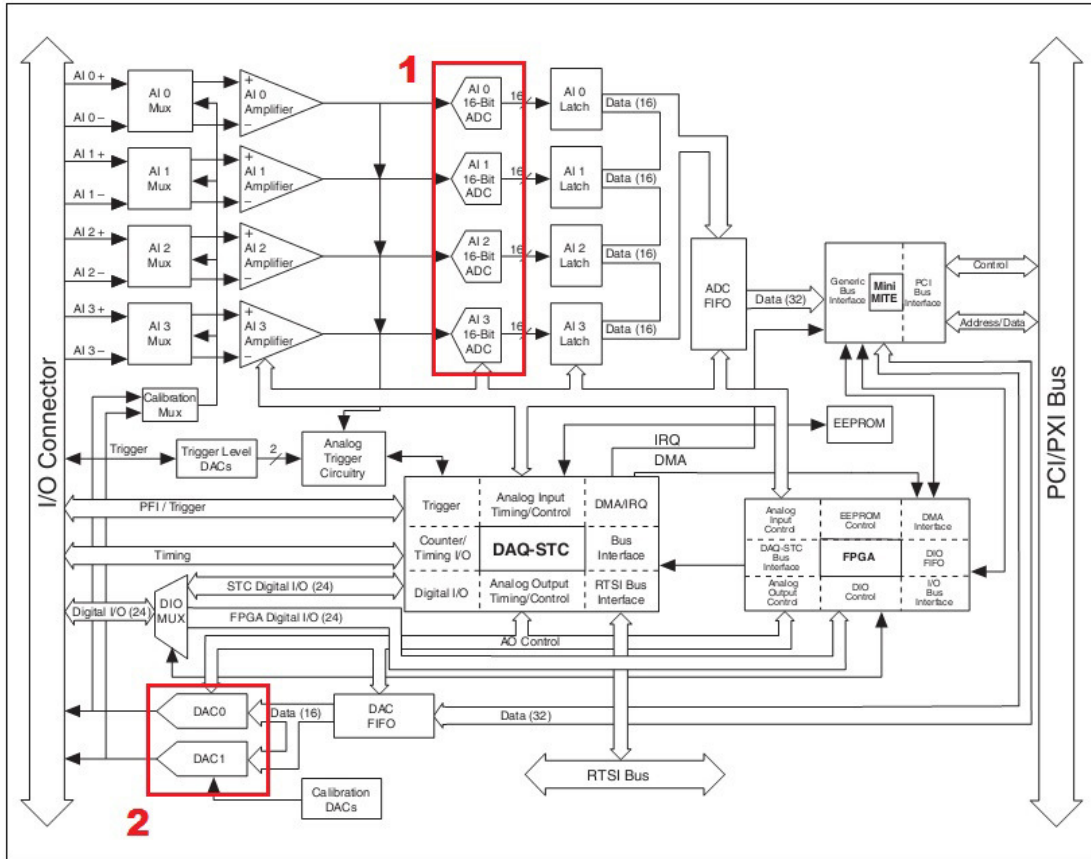


FIG. 19: BLOCK DIAGRAM OF THE MEASUREMENT CARD NI PCI 6120. HIGHLIGHTS 1 AND 2 SHOW THE ANALOGUE-TO-DIGITAL CONVERTERS FOR EACH INPUT CHANNEL AND THE DIGITAL-TO-ANALOGUE CONVERTERS FOR EACH OUTPUT CHANNEL [17].

2.2 Software

The tasks of this thesis were distributed between programs in two different programming languages:

- G
- C++

The G-program was written in the development environment LabVIEW, commercially available from National Instruments and responsible for signal processing from and to the measurement system. The C++ program was written in an Integrated Development Environment (IDE) and responsible for various numerical calculations

2.2.1 LabVIEW

LabVIEW is a development environment for writing a program in the graphical programming language "G". It is simple to operate and a very common choice for the design of small batch applications that take the role of somewhat unique measurement instruments.

A LabVIEW program consists of a Graphical User Interface (GUI) which is called the front panel and a back panel which can be seen as a block diagram of the program. In this block diagram a flowchart of the programs function is being largely drawn by mouse usage on a canvas of infinite size. LabVIEW programs are called Virtual Instruments (VI), their file extension is ".vi". One can also call other VIs from the main program, just as one would do with a subprogram or a function in a program written in a text based language.

The infinite size of the canvas however comfortable during programming makes it almost meaningless to insert and comment the whole source code of the program written in the course of this thesis here as it would give a rather cluttered picture. This was deliberately omitted and the programs basic functions will be described in writing only.

The program written for this thesis runs with LabVIEW 8.2 and the DAQ MX driver version 9.1.1.

The basic principle of what the hysteresograph does is as follows:

- A voltage signal to control the shape, strength and frequency of the H -field is calculated.
- The input and output parameters of the measurement card are set accordingly.
- The measurement is started and the signal is applied to the input of a voltage controlled current amplifier.
- Two voltages proportional to the measurement quantities are measured.
- The measurement is finished and the data are readied for saving in a text file and saved.

The file format used for saving data from a measurement in LabVIEW is “.lvm”. Such a file consists of a header part and a data part. Within the header various parameters of the measurement, such as saving date of the file, the user operating the program and information on the sampling frequency, are listed. The data part contains a time column, two columns for the measured voltages U_1 and U_2 as well as one column for the H -field and one for the B -field.

The signal to control the shape, strength and frequency of the H -field can either be directly calculated in LabVIEW or be read in from a file³.

A quick how-to-use instruction manual for the program can be found in the appendix (Appendix B: HysteresisMeasurements.vi: A short user manual).

2.2.2 C++

A set of programs in C++ was written for improving performance by taking workload from the scientific graphing and analysis software Origin. By performing various compensation calculations with programs written in C++ instead of Origins' LabTalk, performance speed and simplicity of the data analysis process was vastly improved. The resulting program is called drift_corrector. The compensation calculations performed on the data are for example simple drift and offset compensations in the

³ The file format used for reading a custom signal into the program may only be in the tdms-format.

B -field, rudimentary smoothing procedures of noisy signals and calculation of magnetic quantities that are derived from the B and H -field.

Also programs that were derived from drift_corrector (drift_corrector_folder and b_curve) contribute significantly to make data analysis more efficient. They do so by reading a „to-do-list“ from a file and perform drift compensations (drift_corrector_folder) and calculations to generate a commutation curve from a folder full of measurement files (b_curve).

The program „shaper“ is also a program that was derived from drift_corrector but with an additional feature: based on [18] it also calculates the next likely function $H(t)$ to cause a triangular $B(t)$ and saves the voltage that will cause this H -field in an additional two column text file.

The voltage output files have to be formatted to LabVIEW binaries (the before mentioned tdms-format) by importing them to Origin and exporting them from there as LabVIEW tdms-files. This was deliberately done so to introduce a human control point before sending the voltage to the amplifier to omit any damage possible to the amplifier and the sample by undetectable errors which may happen during file saving procedures.

3. Results

Four different samples were examined closer with frequency dependent hysteresis measurements applying different signal shapes $H(t)$ or $B(t)$ and shall be presented in this chapter. One of them was used to check the measurement procedure ($Fe_{75}Al_{25}$), one was used to examine the low signal limits of the system (VP-800-2), the other two ($Fe_{97}Si_3$ and $Fe_{57,3}Ni_{10}Si_{33,3}$) were used to validate the simple loss separation formula

$$\frac{P}{f} = C_0 + C_1 \cdot f + C_2 \cdot \sqrt{f}$$

EQ. 44

The interpretation of the measurement results follows in the next chapter.

3.1 Hysteresis measurements on $Fe_{75}Al_{25}$

To investigate the procedure of measuring with a triangular B -field, a sample made from an iron-aluminium-alloy with 25% aluminium was chosen. The sample has been SPD-treated at room temperature⁴. Frequency dependent hystereses with constant amplitude were measured for triangular H -field as well as for triangular B -field. The frequency dependence of the losses per frequency was evaluated and will be shown in chapter 4.

3.1.1 Hysteresis for triangular H-field

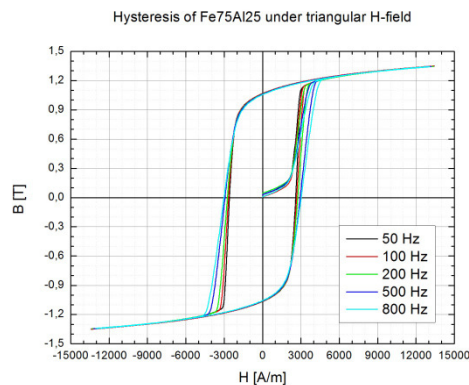


FIG. 20: FREQUENCY DEPENDENT HYSTERESIS OF $Fe_{75}Al_{25}$ UNDER TRIANGULAR H-FIELD

⁴ See [24], chapter 5.1 Hysteresis measurement of HPT treated Fe-Al for further data.

Fig. 20 shows the frequency dependent hysteresis of $Fe_{75}Al_{25}$ under triangular H -field. It clearly shows coercive H -field values in the range of a few thousand amperes per meter and exhibits very little dynamic losses compared to the static losses. The material has an almost Z-shaped hysteresis.

3.1.2 Hysteresis for triangular B-field

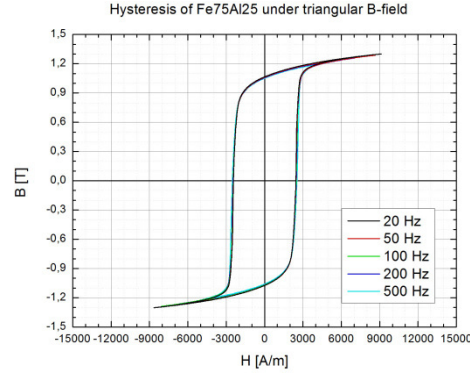


FIG. 21: FREQUENCY DEPENDENT HYSTERESIS OF $Fe_{75}Al_{25}$ UNDER TRIANGULAR B-FIELD

Fig. 21 shows frequency dependent hysteresis measurements of $Fe_{75}Al_{25}$ under triangular B -field. One instantaneously sees that the frequency dependence of the coercivity and dynamic losses becomes “flatter” under triangular B -field than it was under triangular H -field. Later, we will see how the dynamic losses are separated into classical and excess losses. We will do this by plotting the area of the B-H-curve versus the frequency and fit the simple loss separation formula Eq. 35 to it. Thusly we can approximate the classical hysteresis losses by the product of the coefficient C_0 and the frequency and assume the remaining part $(P/f - C_0) * f$ of the losses to be the dynamic losses alone which are purely caused by eddy currents. What we need to do further is, to apply the separation of Eq. 37 according to to ansatz Eq. 41.

This is done in three steps:

- First one needs to calculate the time average over one signal period of $(\partial_t J)^2$ and $|\partial_t J|^{\frac{3}{2}}$ for each measured frequency.

- The second step is to perform a least-square-fit of these two columns to the dynamic losses P_W ⁵.
- The third step is to calculate an estimate of C_1 and C_2 according to

$$C_1(f) = \frac{1}{f^2} A_0 [(\partial_t J)^2](f)$$

EQ. 45

and

$$C_2(f) = \frac{1}{f^{\frac{3}{2}}} A_1 [(\partial_t J)^{\frac{3}{2}}](f)$$

EQ. 46

If one neglects the fact, that the model should only be valid for soft magnetic thin slabs and not semi-hard thin plates, it should be possible anyhow to calculate at least the sign and eventually the order of magnitude of C_1 and C_2 from A_0 and A_1 . If this works out, the model is self-consistent and in a case like the next sub-chapter (3.2 Hysteresis measurements on Fe₉₇Si₃) where a soft magnetic thin plates case is treated, it should be possible to calculate an estimate the conductivity respectively the specific electrical resistance to an order of magnitude.

⁵ Let A_0 be the proportionality factor of $(\partial_t J)^2$ in this fit and A_1 be the proportionality factor of $|\partial_t J|^{\frac{3}{2}}$. For further information on the numerical details, please look in the appendix.

3.2 Hysteresis measurements on $\text{Fe}_{97}\text{Si}_3$

This sample consists of iron with three percent silicon content and is undeformed. Frequency dependent hystereses were measured for triangular H -field, sinusoidal H -field as well as for three different amplitudes of triangular B -field. The frequency dependence of the losses per frequency was calculated and will be shown in chapter 4.

3.2.1 Hysteresis for triangular H-field

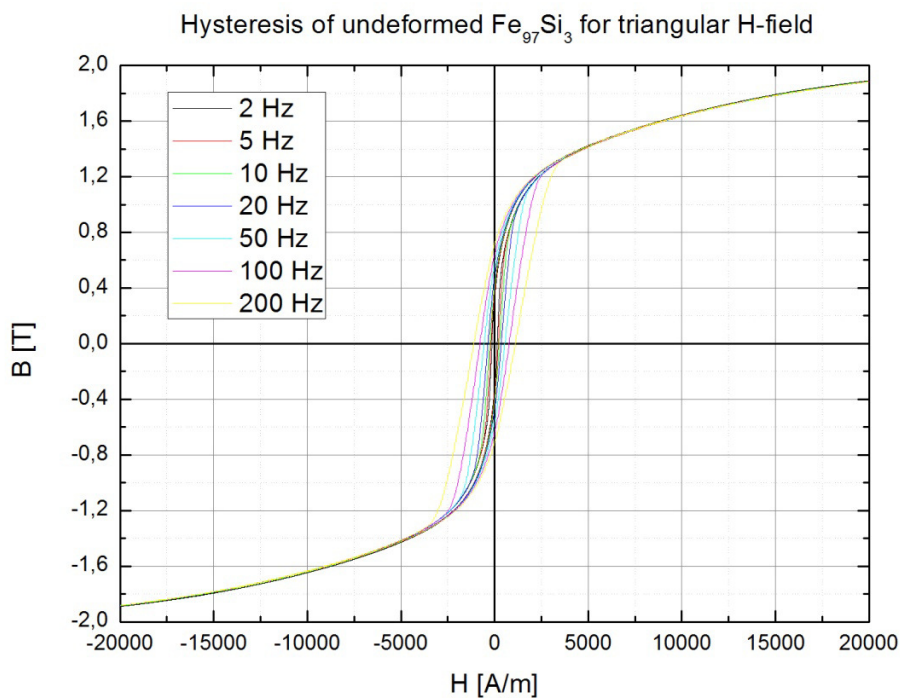


FIG. 22: FREQUENCY DEPENDENT HYSTERESIS OF $\text{Fe}_{97}\text{Si}_3$ UNDER TRIANGULAR H-FIELD

Fig. 22 shows the frequency dependent hysteresis of undeformed $\text{Fe}_{97}\text{Si}_3$ under triangular H -field. The coercive H -field values are clearly in the range below one thousand ampere per meter and so the material is really soft magnetic. The round R-shaped hysteresis indicates that the sample is undeformed or isotropic and magnetic anisotropy effects are negligible.

For these reasons concerning the sample being magnetically soft, isotropic and the thickness being in the range of a thin slab⁶, this sample should fit the requirements

⁶ See Appendix A: Sample characteristics:

of the model best and it should be possible to estimate the specific electrical resistance purely from hysteresis measurements.

3.2.2 Hysteresis for sinusoidal H-field

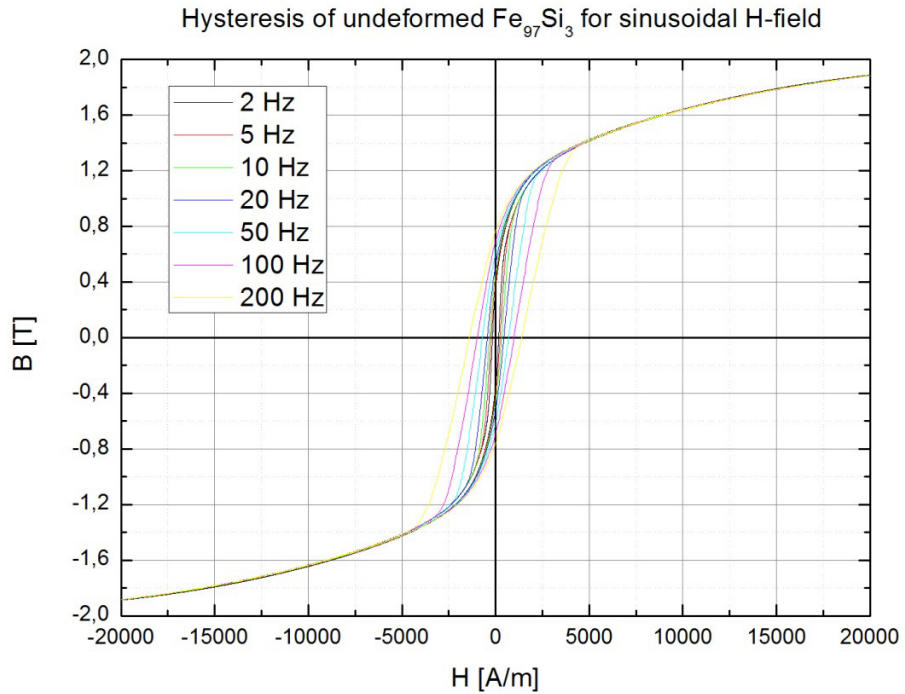


FIG. 23: FREQUENCY DEPENDENT HYSTERESIS OF $Fe_{97}Si_3$ UNDER SINUSOIDAL H-FIELD

To further analyse this samples frequency dependent behaviour of the losses it was also measured under sinusoidal H -field.

3.2.3 Hysteresis for triangular B-field

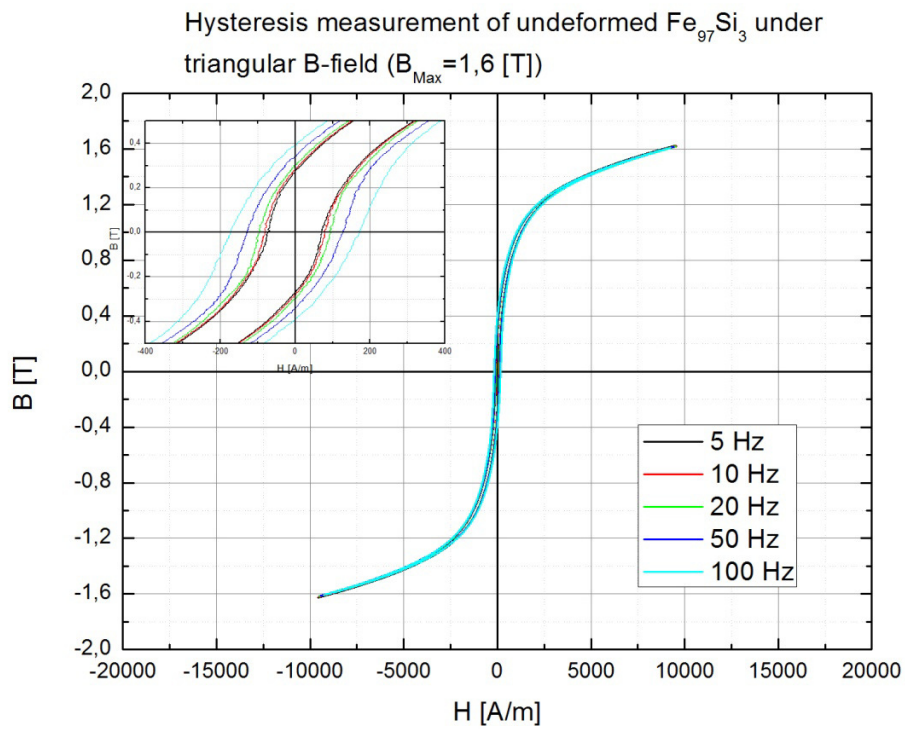


FIG. 24: FREQUENCY DEPENDENT HYSTERESIS OF $Fe_{97}Si_3$ UNDER TRIANGULAR B-FIELD ($B_{MAX}=1,6$ T)

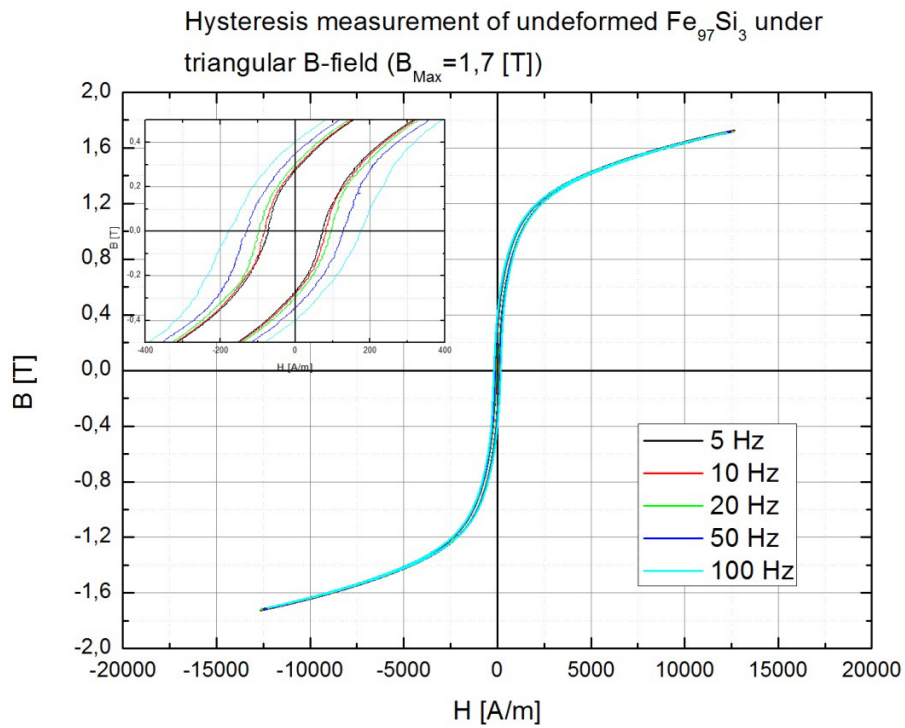


FIG. 25: FREQUENCY DEPENDENT HYSTERESIS OF $Fe_{97}Si_3$ UNDER TRIANGULAR B-FIELD ($B_{MAX}=1,7$ T)

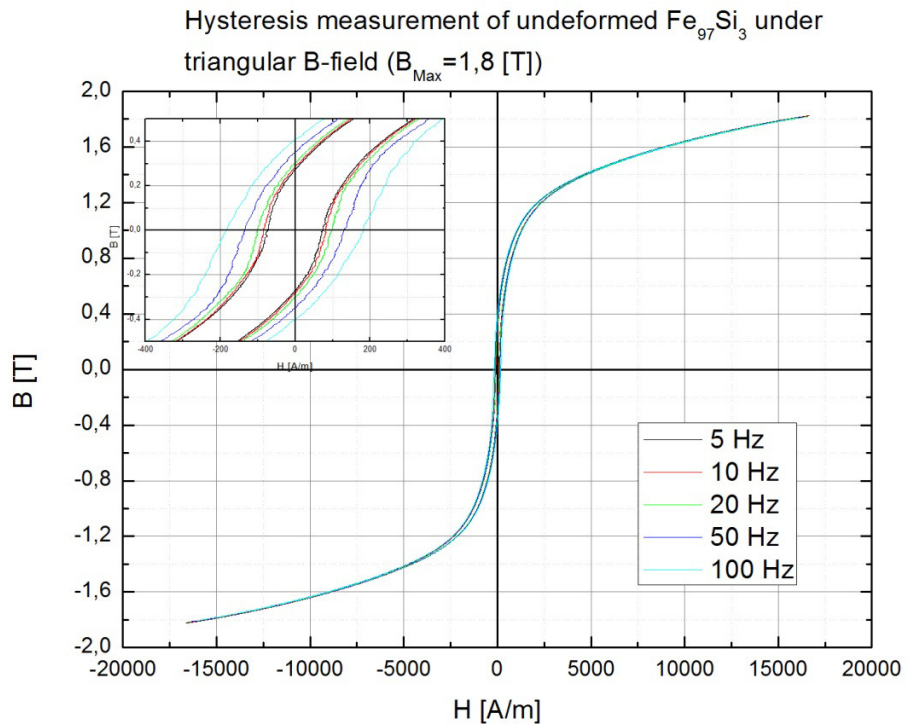


FIG. 26: FREQUENCY DEPENDENT HYSTERESIS OF $Fe_{97}Si_3$ UNDER TRIANGULAR B-FIELD ($B_{MAX} = 1,8$ T)

For triangular B -field, three different amplitudes were chosen for measurement which can be seen in Fig. 24 to Fig. 26. The frequency dependence of the dynamic losses will give some insight on the frequency behaviour of the eddy currents in this sample and the dominant processes involved.

3.3 Hysteresis measurements on $\text{Fe}_{57,3}\text{Ni}_{10}\text{Si}_{33,3}$

The work on this sample was a cooperation of different institutes of Vienna University of Technology and University of Vienna Innovative Materials Group and lead to a poster at the Soft Magnetic Materials conference in Budapest in 2013.

The group from University of Vienna was kind enough to manufacture the sample core, the group of Prof. Bauer of the Institute of Solid State Physics of Vienna University of Technology measured the specific electrical resistivity, Prof. Kubel from the Structure Chemistry group of the Institute of Chemical Technologies and Analytics of the Vienna University of Technology did measure the crystal structure while the author of this thesis did the hysteresis measurements. The results can be seen in the special edition of the IEEE Transactions of Magnetics of the conference [19].

The hysteresis measurements will be explained in the next sub-chapters (3.3.1 to 3.3.3), but a few words need to be said about the sample before discussing the measurement results:

It was necessary to measure the specific resistance because such a high silicon content is very unusual in literature, as adding so much silicon commonly leads to a very brittle material which makes it less interesting for manufacturing. For 300 Kelvin, this value was in the range of 180 to 190 $\mu\Omega m$. Unfortunately, it was not possible to saturate the material as a ring shaped sample. The reason for this is that the ring is rather large. This requires either a high number of primary windings or a very high primary current to get the sample close to saturation. The maximum primary current is limited by the amplifier⁷ while the number of primary windings is among other things limited by geometrical factors and preparation time.

⁷ The maximum output current of the KEPCO BOP100-4M is 4 amperes.

3.3.1 Hysteresis for triangular H-field

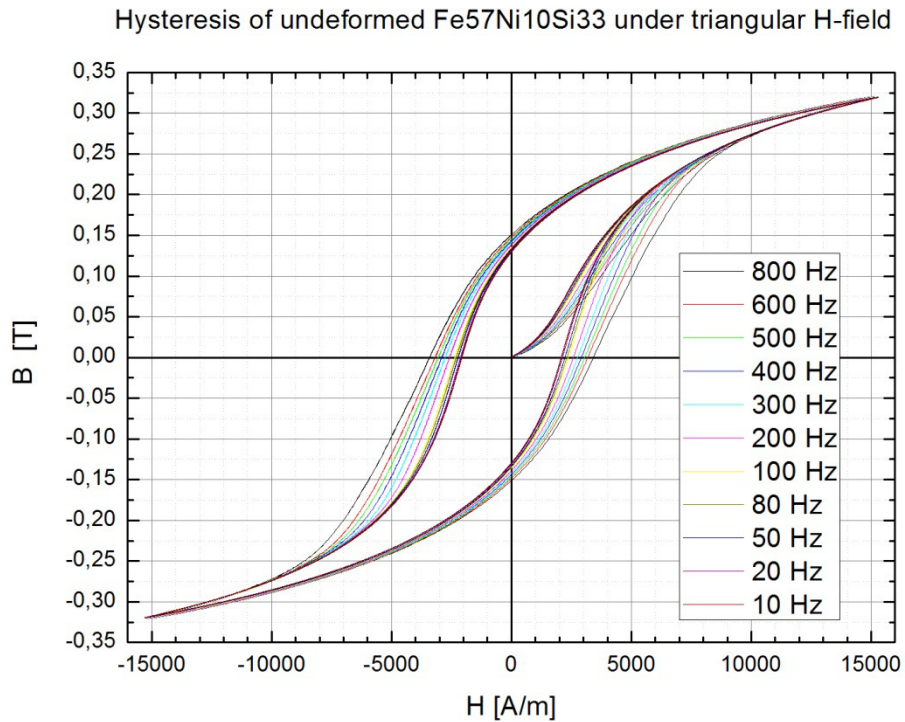


FIG. 27: FREQUENCY DEPENDENT HYSTERESIS FOR $Fe_{56.7}Ni_{10}Si_{33.3}$ UNDER TRIANGULAR H-FIELD

Fig. 27 shows the frequency dependent hysteresis of $Fe_{56.7}Ni_{10}Si_{33.3}$ under triangular H -field. The coercive H -field values are clearly in the range above one thousand ampere per meter and so the material cannot be considered as a good soft magnetic material – it is clearly visible that the loop is far from saturation.

For these reasons concerning the sample being magnetically semi-hard and the thickness being far from being in the range of a thin slab⁸, this sample should not fit the model very well but nevertheless offers a good possibility to investigate the frequency dependent behaviour of not saturated loops with a decent signal to noise ratio.

⁸ See Appendix A: Sample characteristics:

3.3.2 Hysteresis for sinusoidal H-field

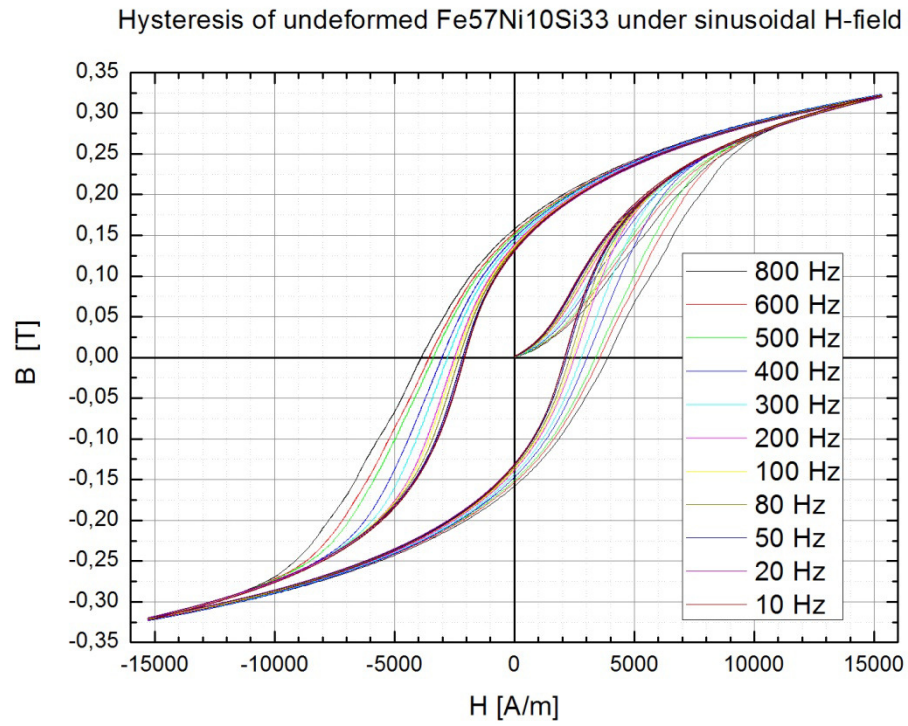


FIG. 28: FREQUENCY DEPENDENT HYSTERESIS FOR $Fe_{56.7}Ni_{10}Si_{33.3}$ UNDER SINUSOIDAL H-FIELD

Fig. 28 shows the frequency dependent measurement of $Fe_{56.7}Ni_{10}Si_{33.3}$ under sinusoidal H -field to investigate the frequency dependent behaviour of the losses under these conditions.

3.3.3 Hysteresis for triangular B-field

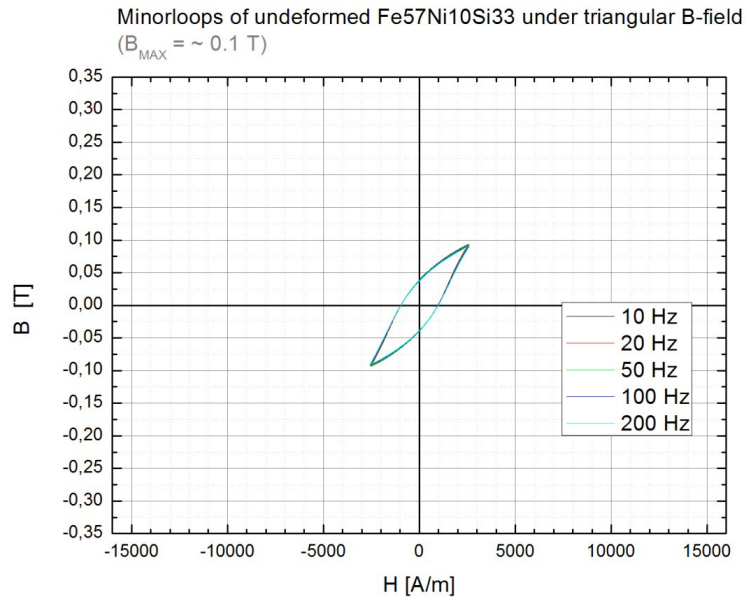


FIG. 29: FREQUENCY DEPENDENT HYSTERESIS OF $Fe_{56.7}Ni_{10}Si_{33.3}$ UNDER TRIANGULAR B-FIELD
($B_{MAX} = 0,1$ T)

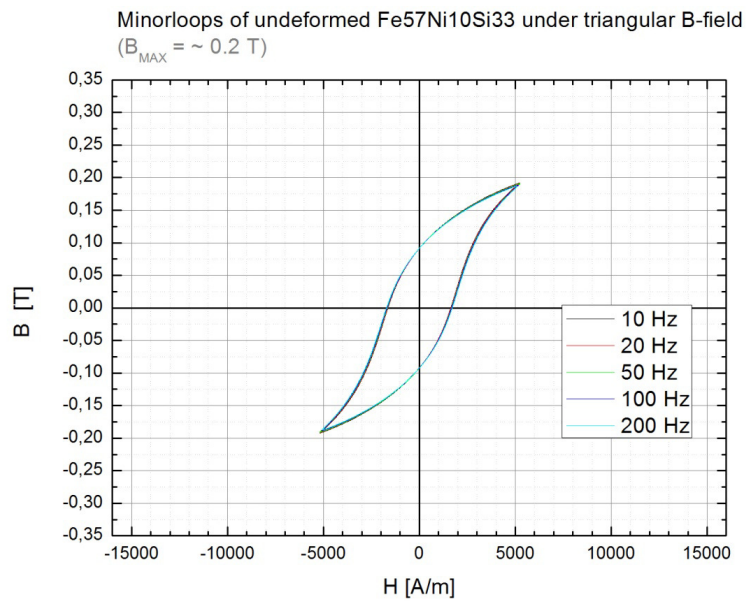


FIG. 30: FREQUENCY DEPENDENT HYSTERESIS OF $Fe_{56.7}Ni_{10}Si_{33.3}$ UNDER TRIANGULAR B-FIELD
($B_{MAX} = 0,2$ T)

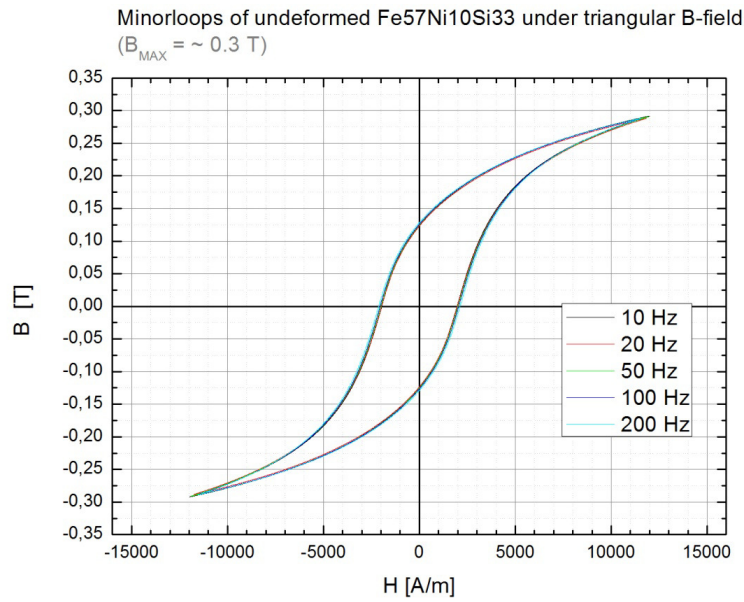


FIG. 31: FREQUENCY DEPENDENT HYSTERESIS OF $Fe_{56.7}Ni_{10}Si_{33.3}$ UNDER TRIANGULAR B-FIELD ($B_{MAX} = 0,3$ T)

For triangular B -field, three different amplitudes were chosen for measurement which can be seen in Fig. 29 to Fig. 31. The frequency dependence of the dynamic losses will also give some insight on the frequency behaviour of the eddy currents in this sample and will be summarized in chapter 4.

3.4 Hysteresis measurements on VP 800-2

The material VITROPERM 800 is a commercially available nano-crystalline soft magnetic material. Its composition is $Fe_xCu_1Nb_3Si_{15,6}B_{6,6}$ ⁹ and it is in the shape of a tape wound core. The tape was manufactured by meltspinning and the shape of the hysteresis was tailored by applying a transversal and a longitudinal field during the crystallisation process. Thusly, the hysteresis for this sample is extremely narrow (ultra soft magnetic) and steep (high permeability). The possibility alone to examine the systems behaviour when working in the single-digit-ampere-per-meter range makes this sample interesting already. Unfortunately, this makes the sample also very sensitive to noise. The high permeability¹⁰ poses an additional challenge, as it results in high inductivity values which in turn reduce the usable bandwidth of the amplifier.

With extreme caution, some measurements were possible nonetheless.

3.4.1 Hysteresis for triangular H-field

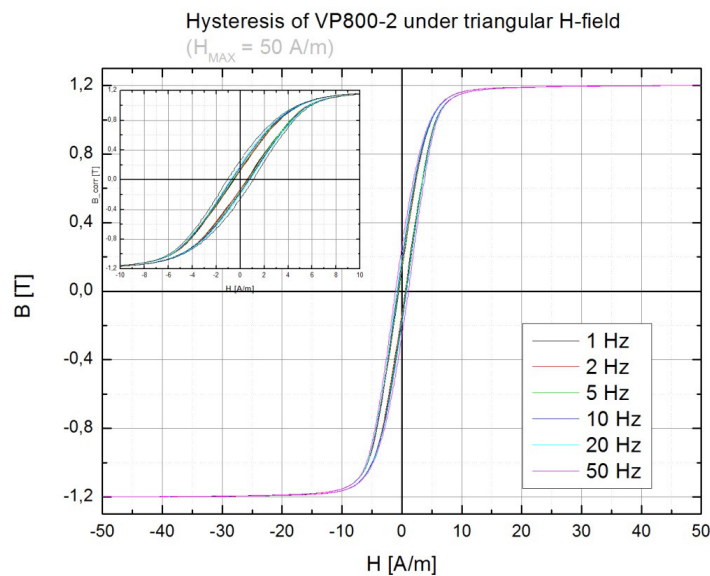


FIG. 32: FREQUENCY DEPENDENT HYSTERESIS OF VP800-2 UNDER TRIANGULAR H-FIELD ($H_{MAX} = 50$ A/M) WITH CLOSEUP-INLAY OF THE DATA AROUND THE ORIGIN

⁹ The numbers give the content of the respective substance in atomic percent. The percentage x of iron is obviously what remains if one subtracts all the other percentages from 100.

¹⁰ The manufacturer states, that this sample has a relative permeability of 151000 which means that even with a primary winding number as low as $N_1=5$ the inductivity of the primary coil will be roughly 4,4 mH.

Fig. 32 shows, that the range of the H -field which is interesting for measurement with triangular B -field is in the single-digit Ampere per meter H -field amplitude range.

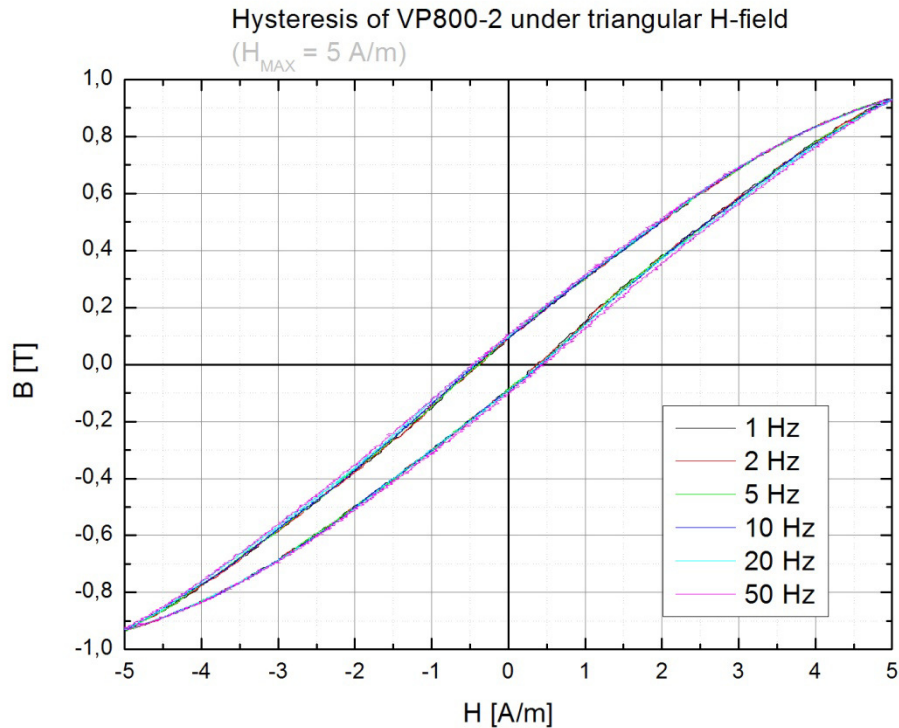


FIG. 33: FREQUENCY DEPENDENT HYSTERESIS OF VP800-2 UNDER TRIANGULAR H-FIELD
($H_{MAX} = 5 \text{ A/M}$)

Fig. 33 shows measurements of VP800-2 under triangular H -field with a reduced amplitude of five Ampere per meter and indicates, that the frequency dependence is low already. One also sees that though it is possible to roughly read the order of magnitude of the coercive H -field that it is nearly impossible to estimate the frequency dependence of the coercive H -field because of the small signals involved and thusly being the most sensitive of all the samples to ambient and system inherent noise.

3.4.2 Hysteresis for triangular B-field

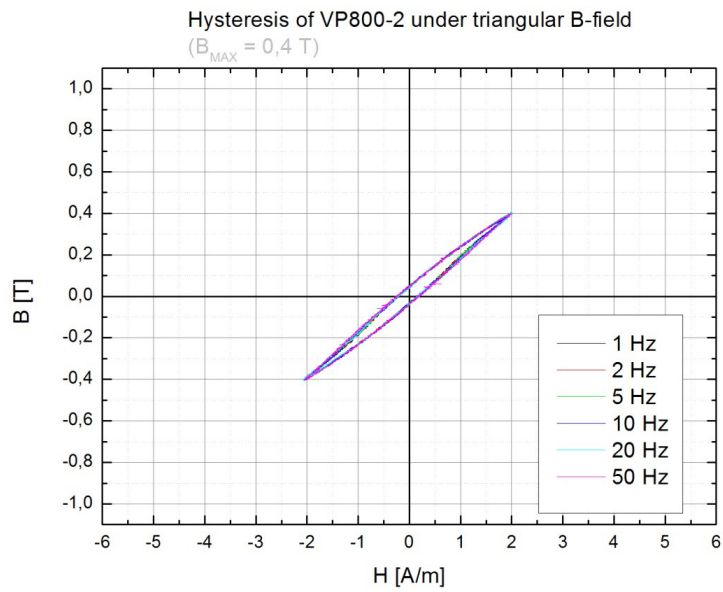


FIG. 34: FREQUENCY DEPENDENT HYSTERESIS OF VP800-2 UNDER TRIANGULAR B-FIELD
($B_{MAX} = 0,4 \text{ T}$)

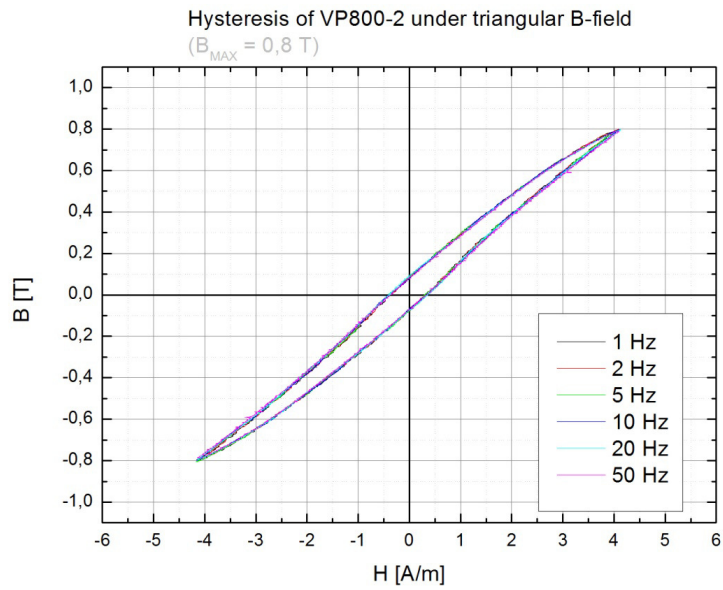


FIG. 35: FREQUENCY DEPENDENT HYSTERESIS OF VP800-2 UNDER TRIANGULAR B-FIELD
($B_{MAX} = 0,8 \text{ T}$)

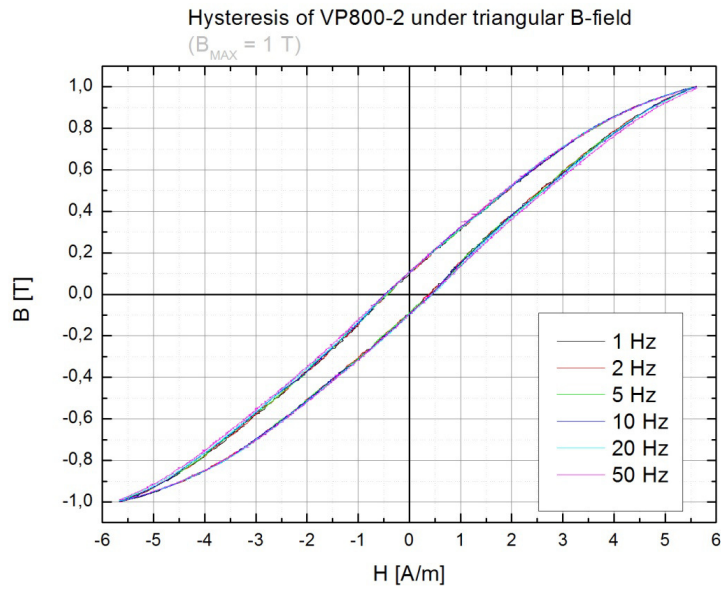


FIG. 36: FREQUENCY DEPENDENT HYSTERESIS OF VP800-2 UNDER TRIANGULAR B-FIELD ($B_{MAX} = 1,0 \text{ T}$)

For triangular B -field, three different amplitudes were chosen for measurement which can be seen in Fig. 34 to Fig. 36. The frequency dependence of the dynamic losses is flattened even more compared to measurements with triangular H -field and will be discussed in chapter 4.

4. Interpretation

This chapter summarizes what can be derived from the measurements presented in chapter 3.

1. It will be shown, how the signals look for the different cases of H -field and B -field shapes. Also it will be shown how the procedure converges in a fast case and in an average case.
2. The permeability values for all the samples will be evaluated so that an estimate of the inductivity of each sample can be calculated. Also, as an example the frequency dependence of the permeability of one sample will be shown.
3. The frequency dependence of the losses of each sample respectively the losses per cycle will be shown and thoroughly analyzed to see if they meet the requirements of the loss model described in chapter 1.3. As mentioned in chapter 3, the time average of the terms proportional to the $\partial_t J$ power 2 and $3/2$ terms over one signal period will be compared to the parameters C_1 and C_2 of the simple loss analyzes formula. For the case where the model applies best, the specific electrical resistance will be calculated and compared to literature values.

4.1 Signal shapes and convergence speed

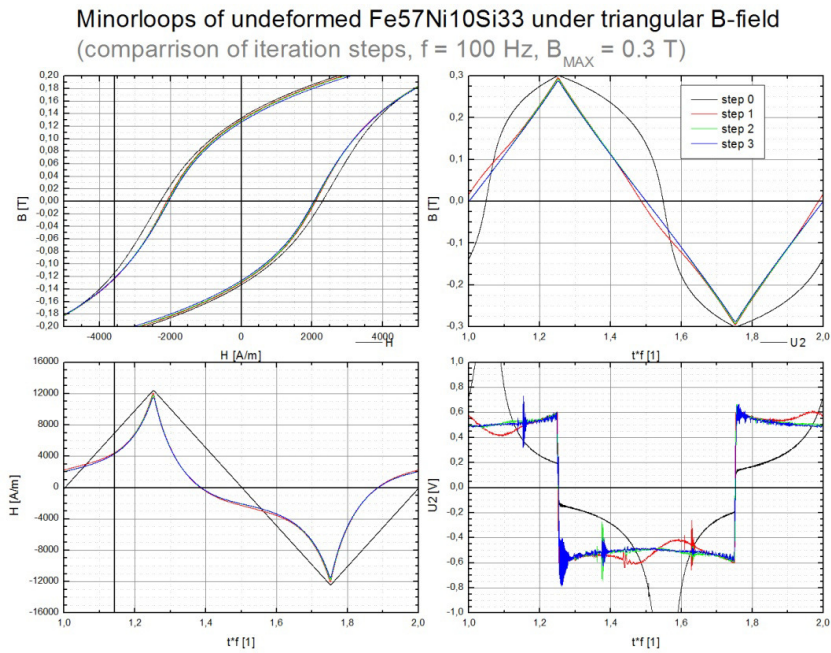


FIG. 37: MINOR LOOPS OF $Fe_{56,7}Ni_{10}Si_{33,3}$ FOR DIFFERENT ITERATION STEPS OF THE TRIANGULAR B-FIELD PROCEDURE¹¹.

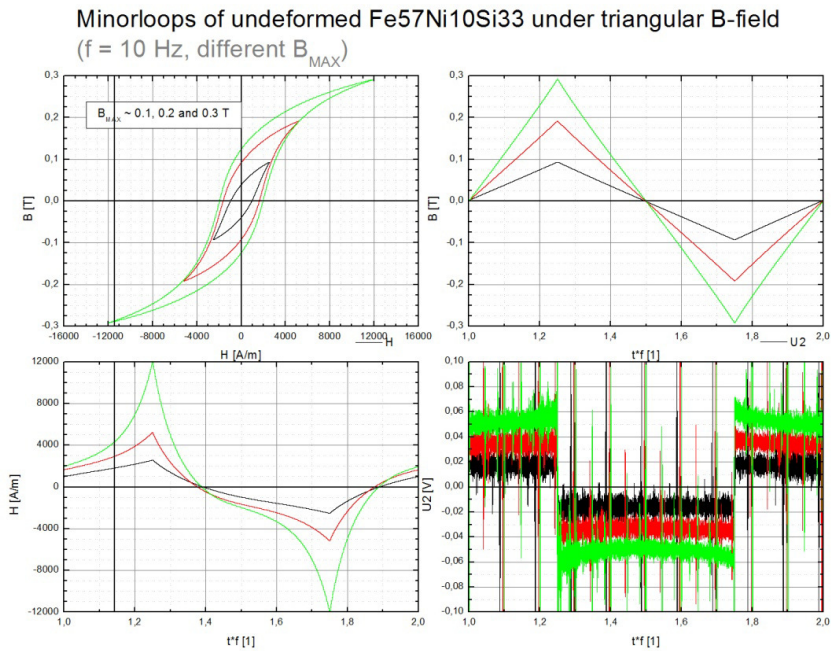


FIG. 38: MINOR LOOPS OF $Fe_{56,7}Ni_{10}Si_{33,3}$ UNDER TRIANGULAR B-FIELD OF 10 HZ AND DIFFERENT B-FIELD AMPLITUDES¹¹.

¹¹ The y-axis is given in time times frequency instead of time to scale it in units of signal periods.

Fig. 37 shows a typical convergence behaviour of the triangular $B(t)$ -field procedure as well as typical signal shapes for both triangular H -field (step 0) and for triangular B -field (step 3). The upper left graph shows a close-up of the minor loops around the origin to show the change in the shape from one iteration to the next of the hysteresis better. The upper right graph shows the evolution of the B -field from triangular H -field (step 0) to a triangular B -field (step 3), the lower left graph shows the same evolution for the H -field signals that cause these B -field signals. The lower right graph shows the evolution of the voltage induced on the secondary side of the sample which is a measure for $\partial_t B$ as it is proportional to it.

Three iteration steps were enough to get the signals of this sample to a crest factor within 1 % of the desired value, which is good. Fig. 39 will show, where it works even faster.

Fig. 38 illustrates how the H -fields look that cause different B -field amplitudes of the same frequency.

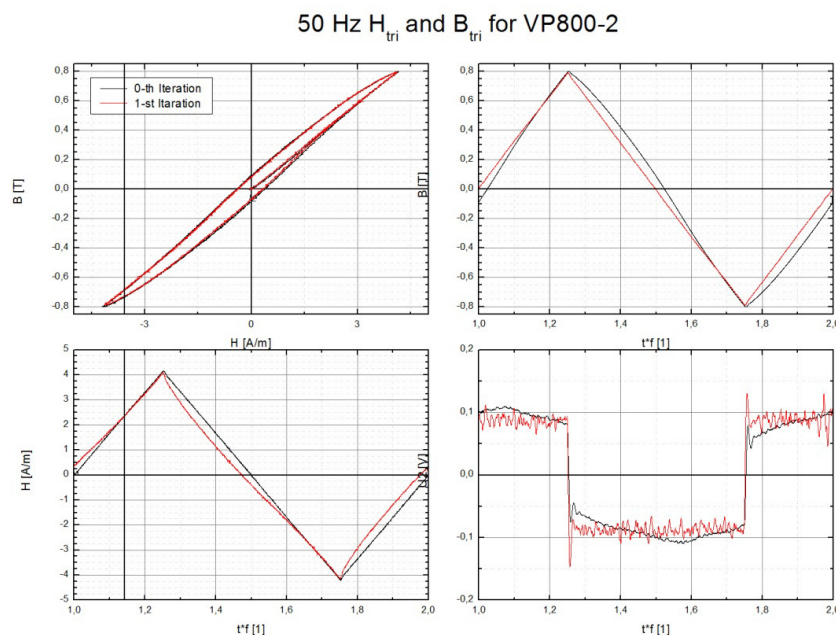


FIG. 39: MINOR LOOPS OF VITROPERM 800-2 UNDER TRIANGULAR H -FIELD AND B -FIELD OF 0,8 T AMPLITUDE FOR 50 HZ¹¹

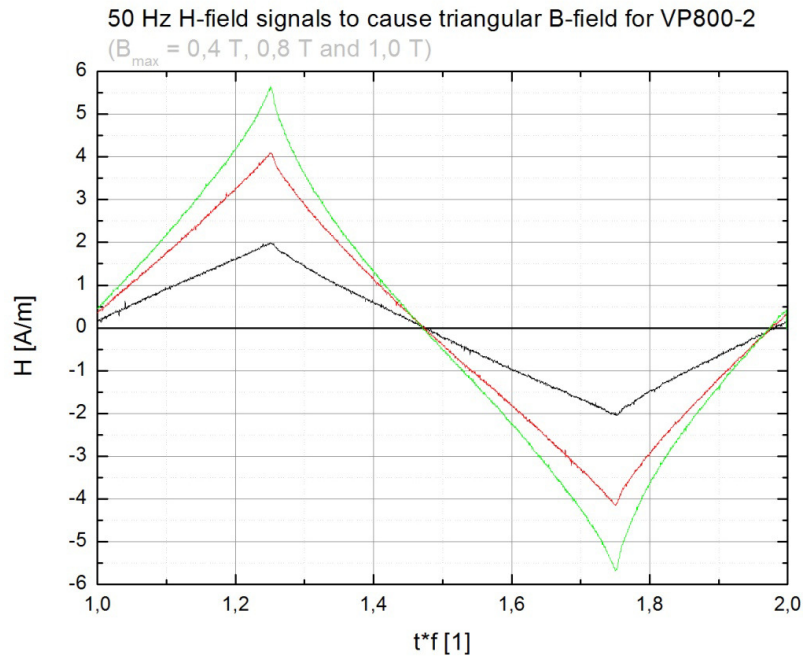


FIG. 40: H-FIELD SIGNALS THAT CAUSE DIFFERENT B-FIELD AMPLITUDES FOR VITROPERM 800-2 AT 50 HZ¹¹

Fig. 39 shows the fastest possible convergence behaviour of the triangular B -field procedure as well as typical signal shapes for both triangular H -field (step 0) and for triangular B -field (step 1). It shows the signals for the procedure to measure VITROPERM 800-2 at a frequency of 50 Hz and an amplitude of 0,8 T.

Fig. 40 shows the H -field signals for this sample that cause different B -field amplitudes at 50 Hz.

It is truly remarkable that the crest factor is within 1 % of the target value for all signal frequencies and amplitudes involved already after one iteration of the procedure. This can be attributed to the sample being made of one of the most magnetically soft materials available. Also it is nanocrystalline and has a nearly frequency independent hysteresis loop due to the rather high specific electrical resistivity in the nanocrystalline state.

4.2 Permeability and inductivity

It is important to know an estimate of the inductivity of each sample to be able to make statements about whether the measurement system is within an operating range of acceptable stability. Depending on this estimate, compensation parameters can be chosen in an educated manner.

The relative permeability is calculated according to

$$\mu_R = \frac{1}{\mu_0} \frac{dB}{dH}$$

EQ. 47

The actual calculation process involves dividing the time derivative signals of B by the respective time derivative signals of H. This poses a big numerical challenge, as even the tiniest noise ratios on the H -field get amplified when calculating the time derivative and thusly resulting in extremely noisy permeability data in samples which are sensitive to bad signal to noise ratios. This basically means, that the more the material is considered soft magnetic and the more the hysteresis can be considered a minor loop the more difficult it gets to show the frequency dependence of the permeability as it is concealed by noise related distortions.

The following figures (Fig. 41 to Fig. 45) show typical frequency and signal shape dependent measurements of the permeability.

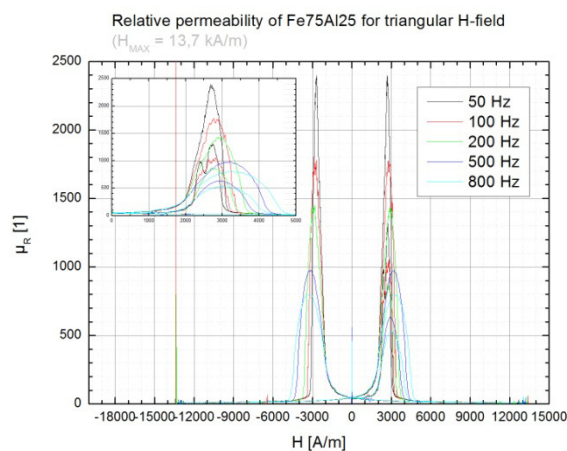


FIG. 41: FREQUENCY DEPENDENT MEASUREMENT OF THE RELATIVE PERMEABILITY OF $FE_{75}AL_{25}$ UNDER TRIANGULAR H-FIELD WITH AN AMPLITUDE OF 13,7 KA/M

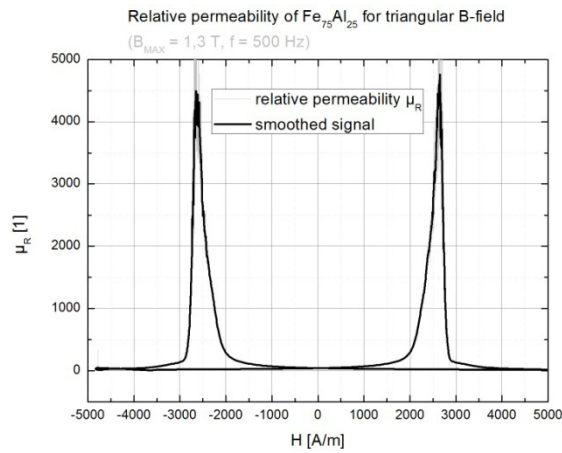


FIG. 42: RELATIVE PERMEABILITY OF FE75AL25 UNDER TRIANGULAR B-FIELD ($f = 500[Hz]$) WITH AN AMPLITUDE OF 1,3 T

Fig. 41 shows the frequency dependent plot of the permeability of Fe₇₅Al₂₅ under a triangular H -field of an amplitude of 13,7 kA/m.

Fig. 42 shows the permeability of the same sample under triangular B -field at a frequency of 500 Hz and an amplitude of 1,3 T. It illustrates how the shape of the permeability curve changes from triangular H -field to triangular B -field: the “peaks” get smaller but higher.

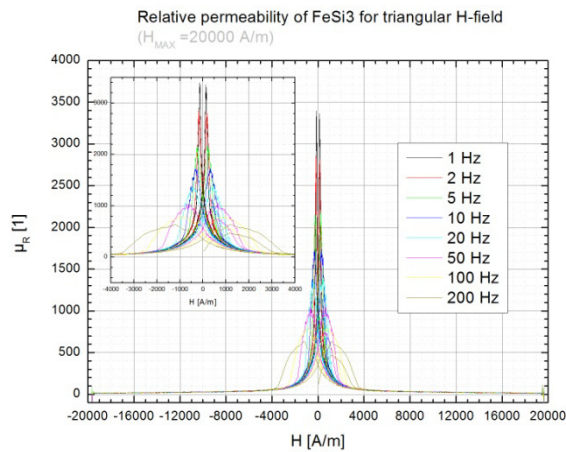


FIG. 43: FREQUENCY DEPENDENT MEASUREMENT OF THE RELATIVE PERMEABILITY OF $Fe_{97}Si_3$ UNDER TRIANGULAR H-FIELD WITH AN AMPLITUDE OF 20 KA/M

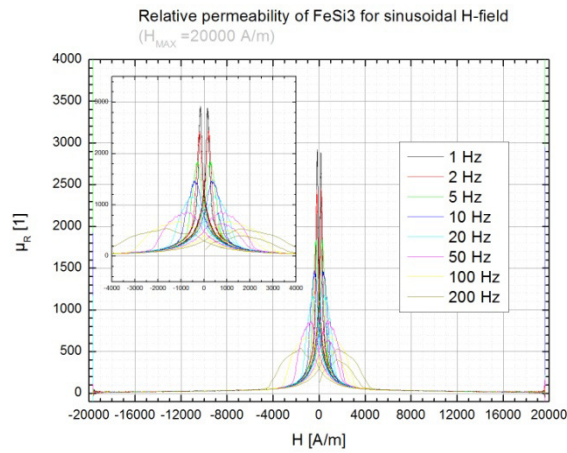


FIG. 44: FREQUENCY DEPENDENT MEASUREMENT OF THE RELATIVE PERMEABILITY OF $Fe_{97}Si_3$ UNDER SINUSOIDAL H -FIELD WITH AN AMPLITUDE OF 20 KA/M

Fig. 43 shows the frequency dependent plot of the permeability of $Fe_{97}Si_3$ under a triangular H -field of an amplitude of 20 kA/m.

Fig. 44 shows the frequency dependent plot of the same samples permeability under sinusoidal H -field of 20 kA/m amplitude. It illustrated how the shape of the permeability curve changes from triangular H -field to sinusoidal H -field: the “peaks” get lower but wider. The inserts in Fig. 43 and Fig. 44 give a better resolution for low fields.

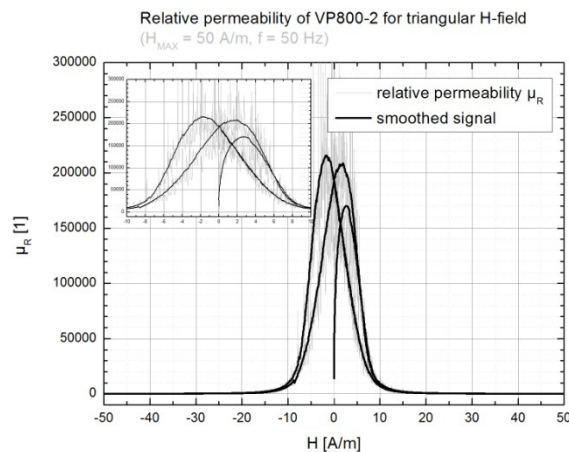


FIG. 45: RELATIVE PERMEABILITY OF VITROPERM 800-2 UNDER TRIANGULAR H -FIELD WITH AN AMPLITUDE OF 50 A/M

Fig. 45 shows the permeability of VITROPEREM 800-2 under a triangular H -field signal with an amplitude of 50 A/m. This beautifully illustrates what it means when

a sample is noise sensitive: Fig. 32 may show a clearly visible hysteresis, yet the noise is enough to conceal the frequency dependence of the permeability and even the shape if the permeability curve itself is not clearly visible without performing a smoothing procedure. The insert in Fig. 45 shows a close-up of the permeability curve to illustrate the shape more articulately.

Tab. 3 summarizes the maxima of the permeability curves for each sample where it was possible to determine them and in what inductivity values L this will result for each samples primary side coil according to Eq. 17. Also, the corresponding H_c is given to indicate the position of the maximum relative permeability μ_R in the plot μ_R versus H

Sample	Shape	f	H_c	μ_R^{12}	L
		[Hz]	[A/m]	[1]	[H]
VP800-2	Triangular H-field	50	1,08	210000	6,186 m
$Fe_{75}Al_{25}$	Triangular H-field	50	2590	2400	327,511 μ
	Triangular H-field	800	3015	800	109,170
	Triangular B-field	500	2526	4600	627,729 μ
$Fe_{97}Si_3$	Triangular H-field	1	117	3300	1,541 m
	Triangular H-field	200	1095	630	294,101 μ
	Sinusoidal H-field	1	130	2600	1,214 m
	Sinusoidal H-field	200	1385	500	233,414 μ
$Fe_{56,7}Ni_{10}Si_{33,3}$	Triangular H-field	10	2059	80	6,678 m
	Triangular H-field	800	3419	50	4,174 m
	Sinusoidal H-field	5	2076	83	6,928 m
	Sinusoidal H-field	800	3895	46	3,840 m

TAB. 3: Summary of the samples inductivities und different signal shapes and frequencies

¹² Maximum of the curve of relative permeability.

4.3 Validation of the loss model

Fe₇₅Al₂₅

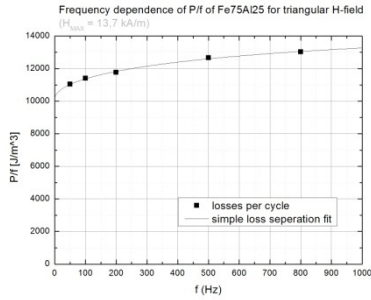


FIG. 46: FREQUENCY DEPENDENCE OF P/f FOR $Fe_{75}Al_{25}$ FOR TRIANGULAR H-FIELD

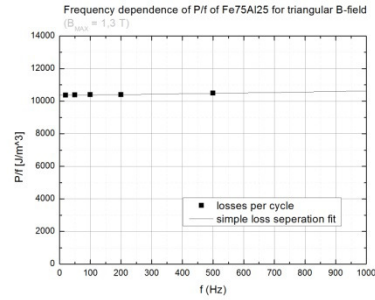


FIG. 47: FREQUENCY DEPENDENCE OF P/f FOR $Fe_{75}Al_{25}$ FOR TRIANGULAR B-FIELD

Fig. 46 and Fig. 47 show the frequency dependence of the loss per cycle for $Fe_{75}Al_{25}$ at triangular H -field (Fig. 46) and triangular B -field (Fig. 47).

Unfortunately, the fit of the simple loss separation ansatz can only serve as an indicator and does not apply here for the separation of the losses according to their origin as can be seen in the following two tables:

	Value	Standard Error
C_0	10101	187
C_1	-1,26	0,70
C_2	140	25

TAB. 4: FIT PARAMETERS OF THE SIMPLE LOSS SEPERATION ANSATZ OF BERTOTTI FOR $Fe_{75}Al_{25}$ UNDER TRIANGULAR H-FIELD (SEE FIG. 46)

	Value	Standard Error
C_0	10385	34,6
C_1	0,369	0,217
C_2	-4,048	6,05

TAB. 5: FIT PARAMETERS OF THE SIMPLE LOSS SEPERATION ANSATZ OF BERTOTTI FOR $Fe_{75}Al_{25}$ UNDER TRIANGULAR B-FIELD (SEE FIG. 47)

The separation ansatz does not give physically meaningful values in this case indicated by the fact, that the parameters responsible for the dynamic losses are negative and the absolute error of those negative fit parameters being in the range of the argument. This leads to the assumption, that Bertottis loss separation ansatz may not be applicable for this system.

Nevertheless the separation ansatz shows to be self consistent already in this case as the signs of C_1 from the simple loss separation ansatz and A_0 from the $(\partial_t J)^2$ averaging process match, just like those of C_2 and A_1 from the $|\partial_t J|^{3/2}$ averaging

process do also match. The estimated values of $C_1(f)$ and $C_2(f)$ however are off by sometimes a few orders of magnitude and vary a great deal which further confirms that this material does not fit the requirements of the loss separation ansatz.

What would improve the quality of the fit is, when the parameter C_1 is forced to be zero

	Value	Standard Error
C_0	10417	91
C_1	0	0
C_2	95,3	5,02

TAB. 6: FIT PARAMETERS OF THE SIMPLE LOSS SEPERATION ANSATZ OF BERTOTTI FOR $Fe_{75}Al_{25}$ UNDER TRIANGULAR H-FIELD WITH C_1 FORCED TO ZERO

	Value	Standard Error
C_0	10332	19
C_1	0	0
C_2	6,026	1,47

TAB. 7: FIT PARAMETERS OF THE SIMPLE LOSS SEPERATION ANSATZ OF BERTOTTI FOR $Fe_{75}Al_{25}$ UNDER TRIANGULAR B-FIELD WITH C_1 FORCED TO ZERO

Fe_{56,7}Ni₁₀Si_{33,3}

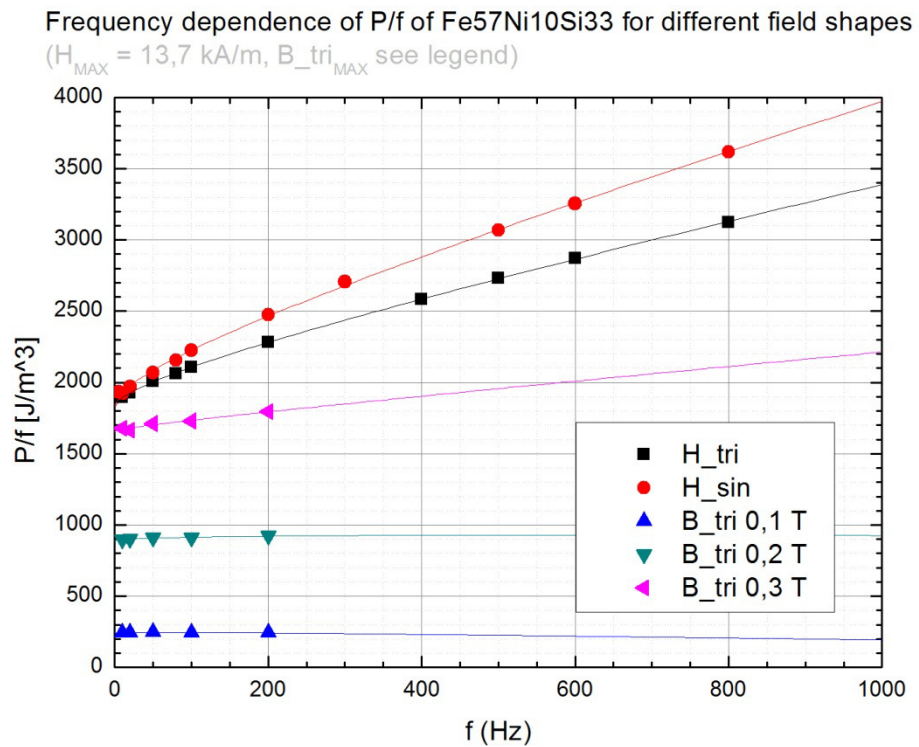


FIG. 48: FREQUENCY DEPENDENCE OF P/f FOR $Fe_{56,7}Ni_{10}Si_{33,3}$ FOR DIFFERENT FIELD SHAPES

Fig. 48 shows the frequency dependence of the loss per cycle for $Fe_{56,7}Ni_{10}Si_{33,3}$ at sinusoidal H -field, triangular H -field and triangular B -field. The parameters for

the separation of the losses (see Eq. 35) according to their origin can be seen in the following five tables:

	Value	Standard Error
C_0	1837	16,6
C_1	1,321	0,094
C_2	25,7	2,85

TAB. 8: FIT PARAMETERS OF THE SIMPLE LOSS SEPERATION ANSATZ OF BERTOTTI FOR $Fe_{56,7}Ni_{10}Si_{33,3}$ UNDER SINUSOIDAL H-FIELD (SEE FIG. 48)

	Value	Standard Error
C_0	1825	6,9
C_1	0,9837	0,0358
C_2	18,31	1,12

TAB. 9: FIT PARAMETERS OF THE SIMPLE LOSS SEPERATION ANSATZ OF BERTOTTI FOR $Fe_{56,7}Ni_{10}Si_{33,3}$ UNDER TRIANGULAR H-FIELD (SEE FIG. 48)

	Value	Standard Error
C_0	1655	31
C_1	0,45	0,48
C_2	3,423	8,44

TAB. 10: FIT PARAMETERS OF THE SIMPLE LOSS SEPERATION ANSATZ OF BERTOTTI FOR $Fe_{56,7}Ni_{10}Si_{33,3}$ UNDER TRIANGULAR B-FIELD WITH AN AMPLITUDE OF 0,3 T (SEE FIG. 48)

	Value	Standard Error
C_0	887	8,9
C_1	-0,0689	0,138
C_2	3,391	2,425

TAB. 11: FIT PARAMETERS OF THE SIMPLE LOSS SEPERATION ANSATZ OF BERTOTTI FOR $Fe_{56,7}Ni_{10}Si_{33,3}$ UNDER TRIANGULAR B-FIELD WITH AN AMPLITUDE OF 0,2 T (SEE FIG. 48)

	Value	Standard Error
C_0	241,9	5,273
C_1	-0,0894	0,0818
C_2	1,302	1,437

TAB. 12: FIT PARAMETERS OF THE SIMPLE LOSS SEPERATION ANSATZ OF BERTOTTI FOR $Fe_{56,7}Ni_{10}Si_{33,3}$ UNDER TRIANGULAR B-FIELD WITH AN AMPLITUDE OF 0,1 T (SEE FIG. 48)

The separation ansatz does give somewhat more physically meaningful values in this case. This is indicated by the fact that the relative error, especially for the factor C_1 which covers the classical eddy current losses, is considerably lower than in the case of $Fe_{75}Al_{25}$. This leads to the assumption, that Bertottis loss separation ansatz may be applicable here for some of the frequency dependent loss measurements.

Those calculations which are not disturbed by the statistical spread of the P/f -values to a degree where the coefficients of the dynamic losses have an error considerably smaller than the argument itself are becoming interesting. Those are the measurement series with triangular H -field and sinusoidal H -field. They may be used to calculate an estimate of the specific resistance:

f	P/f	$(\partial_t J)^2$	$ \partial_t J ^{3/2}$	P_W	$C_1(f, A_0)$	$C_2(f, A_1)$
[Hz]	[J/m ³]			[(J/m ³) * s]	[(J/m ³) * s]	[(J/m ³) * s ^{1/2}]
5	1933,81	153,686	27,801	480,274	2,445	11,476
10	1924,15	601,900	77,525	863,976	2,394	11,314
20	1968,22	2,410 k	219,588	2,609 k	2,397	11,330
50	2067,46	14,943 k	867,340	11,485 k	2,378	11,322
80	2155,81	37,837 k	1,751 k	25,445 k	2,352	11,291
100	2224,49	59,015 k	2,453 k	38,674 k	2,347	11,319
200	2475,11	225,921 k	6,841 k	127,472 k	2,247	11,162
300	2706,02	489,087 k	12,407 k	260,480 k	2,162	11,019
500	3067,79	1,251 M	25,772 k	615,020 k	1,990	10,638
600	3256,05	1,801 M	33,537 k	850,982 k	1,991	10,531
800	3617,79	2,964 M	50,679 k	1,424 M	1,842	10,336

TAB. 13: FREQUENCY DEPENDENT ESTIMATION OF C_1 AND C_2 FOR $Fe_{56,7}Ni_{10}Si_{33,3}$ UNDER SINUSOIDAL H-FIELD

The parameter C_1 is in the same order of magnitude as its counterpart from Tab. 8, so an estimation of the specific electrical resistivity may be attempted here. Also C_2 matches its counterpart at least to a order of magnitude.

The parameters A_0 and A_1 were calculated as described in 3.1.2 and are:

A_0	A_1
397,776 m	4,615

TAB. 14: LEAST SQUARE FIT PARAMETERS TO TAB. 13

Comparing A_0 to Eq. 41 b, where σ is the inverse of the specific electrical resistivity, the estimated specific electrical resistivity ρ for $Fe_{56,7}Ni_{10}Si_{33,3}$ is $5,237 \mu\Omega m$ under sinusoidal H -field. This value is in the same order of magnitude as the at DC-current measured value $1,8 \mu\Omega m$ which is very remarkable. When repeating the calculations for the measurements under triangular H -field¹³, the value for the

¹³ The values for the estimations under triangular H-field look very similar to those in Tab. 13 and it was deliberately omitted to put them into this work, as no real additional information could have been gained from them here.

estimated specific electrical resistivity came out as $5,511\mu\Omega m$. The fact that the calculated specific electric resistivity is always higher than the literature value can be explained considering that the resistivity calculated from the fit is an average value determine from frequency dependent measurements between 1 and 800 Hz. Therefore eddy current contributions are included here.

VITROPERM 800-2

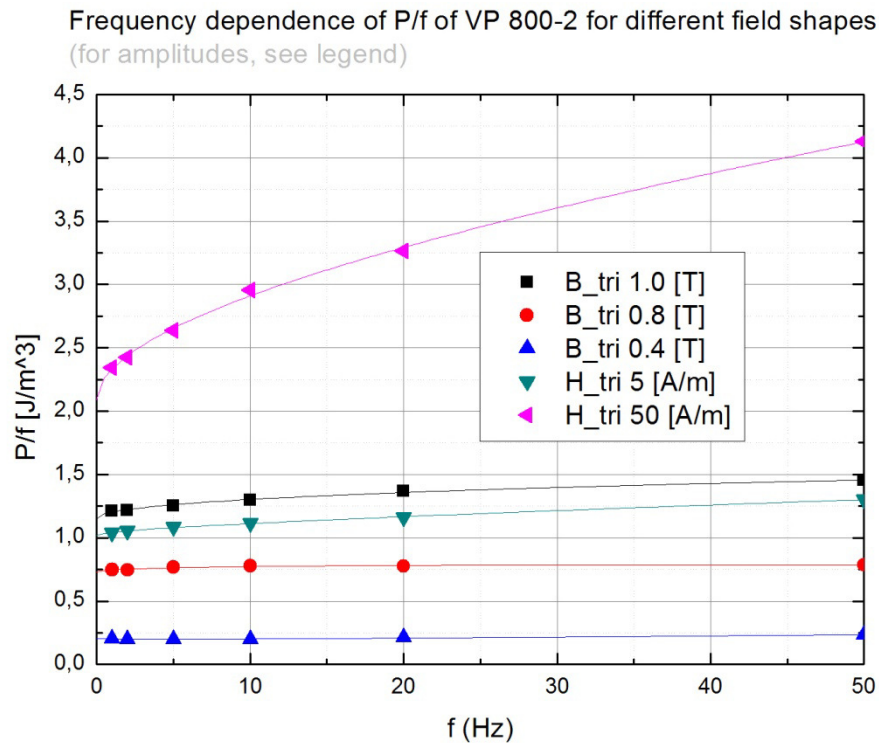


FIG. 49: FREQUENCY DEPENDENCE OF P/f FOR VP800-2 FOR DIFFERENT FIELD SHAPES

Fig. 49 shows the frequency dependence of the loss per cycle for VP800-2 at triangular H -fields of two different amplitudes and triangular B -fields of three different amplitudes. The parameters for the separation of the losses using Eq. 35 can be seen in Tab. 15 to Tab. 19. Although this sample may be used to validate the fact, that the simple loss separation ansatz reflects the separation of the losses according to Eq. 41 pretty well (see Tab. 20 to Tab. 24), the samples fit parameters errors are too big to estimate any physically meaningful value of the electrical resistivity. What could possibly be done to achieve a suitable signal to noise ratio and to elaborate soft magnetic samples better, will also be subject to 5. Summary.

	Value	Standard Error
C_0	2,09	0,045
C_1	0,00737	0,0038
C_2	0,236	0,0311

TAB. 15: FIT PARAMETERS OF THE SIMPLE LOSS SEPERATION ANSATZ OF BERTOTTI FOR VP800-2 UNDER TRIANGULAR H-FIELD OF AMPLITUDE 50 A/M (SEE FIG. 49)

	Value	Standard Error
C_0	1,018	0,0066
C_1	0,00259	0,0005
C_2	0,0217	0,00413

TAB. 16: FIT PARAMETERS OF THE SIMPLE LOSS SEPERATION ANSATZ OF BERTOTTI FOR VP800-2 UNDER TRIANGULAR H-FIELD OF AMPLITUDE 5 A/M (SEE FIG. 49)

	Value	Standard Error
C_0	0,205	0,00526
C_1	0,00137	0,0004
C_2	-0,00536	0,00328

TAB. 17: FIT PARAMETERS OF THE SIMPLE LOSS SEPERATION ANSATZ OF BERTOTTI FOR VP800-2 UNDER TRIANGULAR B-FIELD OF AMPLITUDE 0.4 T (SEE FIG. 49)

	Value	Standard Error
C_0	0,728	0,00973
C_1	-0,00154	0,00073
C_2	0,0189	0,00606

TAB. 18: FIT PARAMETERS OF THE SIMPLE LOSS SEPERATION ANSATZ OF BERTOTTI FOR VP800-2 UNDER TRIANGULAR B-FIELD OF AMPLITUDE 0.8 T (SEE FIG. 49)

	Value	Standard Error
C_0	1,153	0,014
C_1	-0,00116	0,00106
C_2	0,0511	0,0087

TAB. 19: FIT PARAMETERS OF THE SIMPLE LOSS SEPERATION ANSATZ OF BERTOTTI FOR VP800-2 UNDER TRIANGULAR B-FIELD OF AMPLITUDE 1.0 T (SEE FIG. 49)

f	P/f	$(\overline{\partial_t J})^2$	$ \overline{\partial_t J} ^{3/2}$	P_W	$C_1(f, A_0)$	$C_2(f, A_1)$
[Hz]	[J/m ³]			[(J/m ³) * s]	[(J/m ³) * s]	[(J/m ³) * s ^{1/2}]
1	2,342744	82,576	13,542	0,252	3,486 m	0,117
2	2,424599	663,103	76,718	0,668	6,997 m	0,234
5	2,637158	4147,657	303,044	2,733	7,003 m	0,234
10	2,955990	16632,404	857,591	8,655	7,021 m	0,234
20	3,263909	66870,067	2428,826	23,468	7,056 m	0,234
50	4,130202	431146,425	9721,032	101,985	7,279 m	0,237

TAB. 20: FREQUENCY DEPENDENT ESTIMATION OF C_1 AND C_2 FOR VP800-2 UNDER TRIANGULAR H-FIELD OF AMPLITUDE 50 A/M

f	P/f	$(\overline{\partial_t J})^2$	$ \overline{\partial_t J} ^{3/2}$	P_W	$C_1(f, A_0)$	$C_2(f, A_1)$
[Hz]	[J/m ³]			[(J/m ³) * s]	[(J/m ³) * s]	[(J/m ³) * s ^{1/2}]
1	1,03996	8,561	3,927	0,022	1,770 m	10,292 m
2	1,05446	61,339	21,173	0,072	3,170 m	19,620 m
5	1,08205	367,690	82,318	0,319	3,040 m	19,298 m
10	1,11695	1456,262	231,669	0,987	3,010 m	19,201 m
20	1,16152	5806,095	654,279	2,866	3,000 m	19,173 m
50	1,30249	36075,844	2575,913	14,214	2,983 m	19,096 m

TAB. 21: FREQUENCY DEPENDENT ESTIMATION OF C_1 AND C_2 FOR VP800-2 UNDER TRIANGULAR H-FIELD OF AMPLITUDE 5 A/M

f	P/f	$(\overline{\partial_t J})^2$	$ \overline{\partial_t J} ^{3/2}$	P_W	$C_1(f, A_0)$	$C_2(f, A_1)$
[Hz]	[J/m ³]			[(J/m ³) * s]	[(J/m ³) * s]	[(J/m ³) * s ^{1/2}]
1	1,21132	14,966	6,470	0,059	-1,406 m	43,275 m
2	1,21756	78,539	24,730	0,130	-1,845 m	58,481 m
5	1,25357	485,423	97,170	0,505	-1,824 m	58,133 m
10	1,29851	1752,920	262,122	1,459	-1,647 m	55,443 m
20	1,36776	6561,741	721,361	4,304	-1,541 m	53,945 m
50	1,45338	39808,963	2809,106	15,040	-1,496 m	53,144 m

TAB. 22: FREQUENCY DEPENDENT ESTIMATION OF C_1 AND C_2 FOR VP800-2 UNDER TRIANGULAR B-FIELD OF AMPLITUDE 1,0 T

f	P/f	$(\overline{\partial_t J})^2$	$ \overline{\partial_t J} ^{3/2}$	P_W	$C_1(f, A_0)$	$C_2(f, A_1)$
[Hz]	[J/m ³]			[(J/m ³) * s]	[(J/m ³) * s]	[(J/m ³) * s ^{1/2}]
1	0,74826	12,802	5,403	0,020	-1,445 m	15,589 m
2	0,74444	59,767	19,378	0,032	-1,687 m	19,768 m
5	0,76742	357,320	74,959	0,196	-1,614 m	19,345 m
10	0,77728	1178,263	191,408	0,491	-1,330 m	17,465 m
20	0,77675	4235,754	516,961	0,971	-1,195 m	16,677 m
50	0,78625	25292,201	1994,254	2,903	-1,142 m	16,275 m

TAB. 23: FREQUENCY DEPENDENT ESTIMATION OF C_1 AND C_2 FOR VP800-2 UNDER TRIANGULAR B-FIELD OF AMPLITUDE 0,8 T

f	P/f	$\overline{(\partial_t J)^2}$	$\overline{ \partial_t J ^{3/2}}$	P_W	$C_1(f, A_0)$	$C_2(f, A_1)$
[Hz]	[J/m ³]			[(J/m ³) * s]	[(J/m ³) * s]	[(J/m ³) * s ^{1/2}]
1	0,20334	9,454	3,970	-0,002	4,519 m	-9,641 m
2	0,19982	36,938	12,314	-0,010	4,415 m	-10,571 m
5	0,19684	175,579	41,895	-0,041	3,357 m	-9,099 m
10	0,19932	440,125	85,608	-0,057	2,104 m	-6,573 m
20	0,21260	1229,645	196,927	0,152	1,470 m	-5,346 m
50	0,23441	6858,680	742,755	1,472	1,312 m	-5,101 m

TAB. 24: FREQUENCY DEPENDENT ESTIMATION OF C_1 AND C_2 FOR VP800-2 UNDER TRIANGULAR B-FIELD OF AMPLITUDE 0,4 T

The parameters obtained from the least square fits corresponding to Tab. 20 to Tab. 24 are summarized below:

Name	A_0	A_1
Triangular H-field 50 A/m	42,210 μ	8,617 m
Triangular H-field 5 A/m	206,700 μ	2,621 m
Triangular B-field 1,0 T	-93,961 μ	6,689 m
Triangular B-field 0,8 T	-112,890 μ	2,885 m
Triangular B-field 0,4 T	478,055 μ	-2,428 m

TAB. 25: LEAST SQUARE FIT PARAMETERS FOR LOSS EVALUATION OF VP800-2 UNDER DIFFERENT FIELD

Tab. 20 to Tab. 24 give values for C_1 and C_2 in the same order of magnitude as Tab. 15 to Tab. 19 do, which can only be the case if Eq. 17, the simple loss separation ansatz, captures the loss separation according to Eq. 37 and Eq. 41, the averaging process over the $\partial_t J$ proportional power terms, in a sufficient manner.

Fe₉₇Si₃

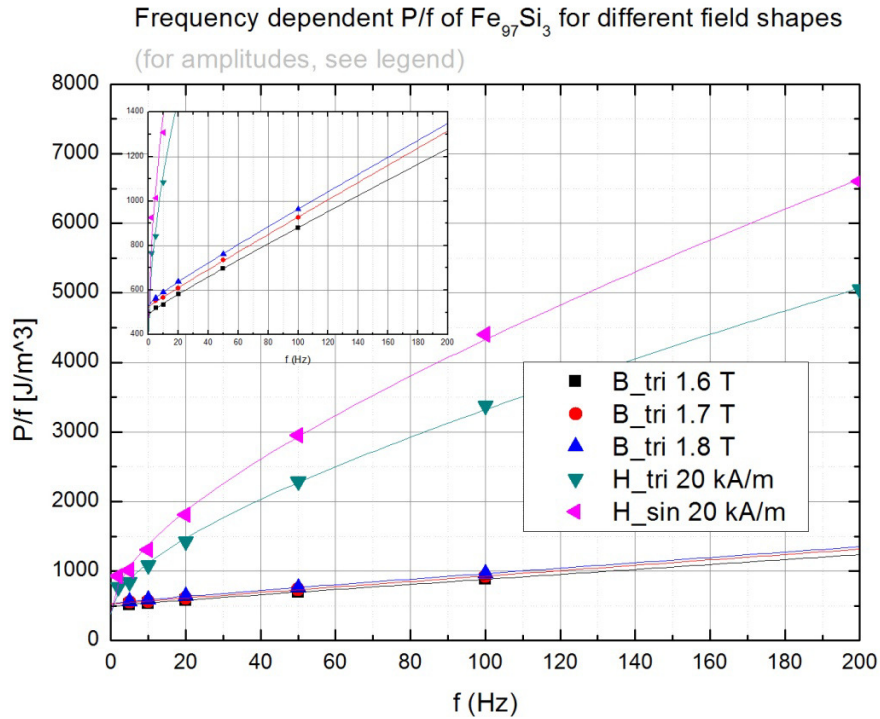


FIG. 50: FREQUENCY DEPENDENCE OF P/f FOR $Fe_{97}Si_3$ FOR DIFFERENT FIELD SHAPES

Fig. 50 shows the frequency dependence of the loss per cycle for $Fe_{97}Si_3$ under sinusoidal and triangular H -field of an amplitude of 20 kA/m and triangular B -field at three different amplitudes. The parameters for the separation of the losses according to their origin can be seen in Tab. 26 to Tab. 30. In Tab. 31 to Tab. 35 it can be seen, that this sample may not only be used to validate the relationship between the already mentioned averaging process and the simple loss separation ansatz, but also that this sample meets the requirements of the model the best so far. This is evident for example by the fact that the relative errors of C_1 are the lowest so far in the simple loss separation ansatz¹⁴ (see Tab. 26 to Tab. 30) and are reproduced the best so far by the averaging process (Tab. 31 to Tab. 35) with minimal statistical spread among themselves.

¹⁴ The relative errors are never higher than twenty percent in this case, in the important cases of triangular B-field they are even lower than ten percent.

	Value	Standard Error
C_0	389,3	104,9
C_1	11,6	2,3
C_2	277,7	35,9

TAB. 26: FIT PARAMETERS OF THE SIMPLE LOSS SEPERATION ANSATZ OF BERTOTTI FOR $Fe_{97}Si_3$ UNDER SINUSOIDAL H-FIELD OF AMPLITUDE 20 KA/M (SEE FIG. 50)

	Value	Standard Error
C_0	384,5	68,1
C_1	9,11	1,5
C_2	202,5	23,35

TAB. 27: FIT PARAMETERS OF THE SIMPLE LOSS SEPERATION ANSATZ OF BERTOTTI FOR $Fe_{97}Si_3$ UNDER TRIANGULAR H-FIELD OF AMPLITUDE 20 KA/M (SEE FIG. 50)

	Value	Standard Error
C_0	527,9	5,05
C_1	3,49	0,159
C_2	8,7	1,97

TAB. 28: FIT PARAMETERS OF THE SIMPLE LOSS SEPERATION ANSATZ OF BERTOTTI FOR $Fe_{97}Si_3$ UNDER TRIANGULAR B-FIELD OF AMPLITUDE 20 1,8 T (SEE FIG. 50)

	Value	Standard Error
C_0	521,6	11,7
C_1	3,73	0,368
C_2	3,35	4,59

TAB. 29: FIT PARAMETERS OF THE SIMPLE LOSS SEPERATION ANSATZ OF BERTOTTI FOR $Fe_{97}Si_3$ UNDER TRIANGULAR B-FIELD OF AMPLITUDE 20 1,7 T (SEE FIG. 50)

	Value	Standard Error
C_0	485	10,3
C_1	3,27	0,322
C_2	6,9	4,01

TAB. 30: FIT PARAMETERS OF THE SIMPLE LOSS SEPERATION ANSATZ OF BERTOTTI FOR $Fe_{97}Si_3$ UNDER TRIANGULAR B-FIELD OF AMPLITUDE 20 1,6 T (SEE FIG. 50)

f	P/f	$\overline{(\partial_t J)^2}$	$ \overline{\partial_t J} ^{3/2}$	P_W	$C_1(f, A_0)$	$C_2(f, A_1)$
[Hz]	[J/m ³]			[(J/m ³) * s]	[(J/m ³) * s]	[(J/m ³) * s ^{1/2}]
2	926,203	3,023 k	171,430	1,074 k	48,783	181,908
5	1014,163	17,037 k	655,261	3,124 k	43,997	175,901
10	1307,354	61,890 k	1,794 k	9,181 k	39,956	170,270
20	1808,510	221,297 k	4,877 k	28,384 k	35,717	163,646
50	2953,581	1,160 M	18,043 k	128,215 k	29,947	153,169
100	4405,493	3,977 M	48,041 k	401,621 k	25,673	144,187
200	6602,881	13,366 M	126,587 k	1,243 M	21,573	134,324

TAB. 31: FREQUENCY DEPENDENT ESTIMATION OF C_1 AND C_2 FOR $Fe_{97}Si_3$ UNDER SINUSOIDAL H-FIELD OF AMPLITUDE 20 KA/M

f	P/f	$\overline{(\partial_t J)^2}$	$ \overline{\partial_t J} ^{3/2}$	P_W	$C_1(f, A_0)$	$C_2(f, A_1)$
[Hz]	[J/m ³]			[(J/m ³) * s]	[(J/m ³) * s]	[(J/m ³) * s ^{1/2}]
2	766,224	2,013 k	139,484	763,367	33,241	138,577
5	842,786	11,430 k	534,700	2,291 k	30,202	134,389
10	1083,662	41,938 k	1,470 k	6,991 k	27,703	130,650
20	1423,564	151,663 k	4,017 k	20,780 k	25,046	126,218
50	2287,470	808,187 k	14,991 k	95,147 k	21,354	119,146
100	3372,600	2,808 M	40,189 k	298,806 k	18,551	112,932
200	5048,046	9,581 M	106,726 k	932,701 k	15,822	106,031

TAB. 32: FREQUENCY DEPENDENT ESTIMATION OF C_1 AND C_2 FOR $Fe_{97}Si_3$ UNDER TRIANGULAR H-FIELD OF AMPLITUDE 20 KA/M

f	P/f	$\overline{(\partial_t J)^2}$	$ \overline{\partial_t J} ^{3/2}$	P_W	$C_1(f, A_0)$	$C_2(f, A_1)$
[Hz]	[J/m ³]			[(J/m ³) * s]	[(J/m ³) * s]	[(J/m ³) * s ^{1/2}]
5	563,412	1,315 k	217,421	177,568	3,699	7,475
10	591,487	5,234 k	612,997	635,891	3,682	7,451
20	638,067	20,834 k	1,729 k	2,203 k	3,664	7,431
50	762,169	129,848 k	6,819 k	11,714 k	3,654	7,414
100	964,551	515,788 k	19,184 k	43,665 k	3,628	7,374

TAB. 33: FREQUENCY DEPENDENT ESTIMATION OF C_1 AND C_2 FOR $Fe_{97}Si_3$ UNDER TRIANGULAR B-FIELD OF AMPLITUDE 1,8 T

f	P/f	$\overline{(\partial_t J)^2}$	$ \overline{\partial_t J} ^{3/2}$	P_W	$C_1(f, A_0)$	$C_2(f, A_1)$
[Hz]	[J/m ³]			[(J/m ³) * s]	[(J/m ³) * s]	[(J/m ³) * s ^{1/2}]
5	551,321	1,184 k	200,837	148,693	3,721	4,290
10	565,661	4,682 k	564,259	440,786	3,679	4,262
20	608,864	18,706 k	1,595 k	1,746 k	3,675	4,259
50	735,525	116,256 k	6,279 k	10,697 k	3,654	4,242
100	926,969	462,344 k	17,674 k	40,539 k	3,633	4,221

TAB. 34: FREQUENCY DEPENDENT ESTIMATION OF C_1 AND C_2 FOR $Fe_{97}Si_3$ UNDER TRIANGULAR B-FIELD OF AMPLITUDE 1,7 T

f	P/f	$\overline{(\partial_t J)^2}$	$ \overline{\partial_t J} ^{3/2}$	P_W	$C_1(f, A_0)$	$C_2(f, A_1)$
[Hz]	[J/m ³]			[(J/m ³) * s]	[(J/m ³) * s]	[(J/m ³) * s ^{1/2}]
5	519,763	1,055 k	184,068	173,774	3,335	7,099
10	534,534	4,175 k	517,633	495,265	3,300	7,058
20	582,684	16,622 k	1,460 k	1,954 k	3,285	7,037
50	698,181	103,385 k	5,751 k	10,659 k	3,269	7,013
100	880,444	411,841 k	16,208 k	39,544 k	3,256	6,989

TAB. 35: FREQUENCY DEPENDENT ESTIMATION OF C_1 AND C_2 FOR $Fe_{97}Si_3$ UNDER TRIANGULAR B-FIELD OF AMPLITUDE 1,6 T

The parameters obtained from the least square fits corresponding to Tab. 31 to Tab. 35 are summarized below and extended by the value of the specific electrical resistance that results from each A_0 value:

Name	A_0	A_1	$\rho(A_0)$
Sinusoidal H-field 20 kA/m	64,560 m	3,001	0,867 $\mu\Omega m$
Triangular H-field 20 kA/m	66,057 m	2,810	0,848 $\mu\Omega m$
Triangular B-field 1,8 T	70,347 m	384,380 m	0,796 $\mu\Omega m$
Triangular B-field 1,7 T	78,574 m	238,839 m	0,713 $\mu\Omega m$
Triangular B-field 1,6 T	79,051 m	431,182 m	0,708 $\mu\Omega m$

TAB. 36: LEAST SQUARE FIT PARAMETERS FOR LOSS EVALUATION OF $Fe_{97}Si_3$ UNDER DIFFERENT FIELD SHAPES WITH THE SPECIFIC ELECTRICAL RESISTIVITY RESULTING FROM THE RESPECTIVE A_0 AND THE SLAB THICKNESS

Tab. 31 to Tab. 35 give values for C_1 and C_2 almost exactly as in the corresponding Tab. 26 to Tab. 30 which not only further confirms the strong correlation between the simple loss separation ansatz from Eq. 17 and the complex separation of Eq. 37 according to the separation from Eq. 41, but shows two more important things:

- The relative error of C_1 is lowest for frequency dependent measurements with triangular B -field.
- The specific electrical resistivity ρ may be estimated for this sample from A_0 because this sample meets the requirements of the loss separation model so close.

The question is now, how close are these values to the real ones? The answer is very simple, because iron with three percent silicon is the most common transformer steel base alloy and so it is well known, that the specific electrical resistivity ρ of iron with three percent silicon is $\sim 0,4 \mu\Omega m$. So the best estimation (triangular B -field with an amplitude of 1,6 T) meets this very closely. Also it should be considered here that the fact that the calculated specific electric resistivity is always higher than the literature value can be explained taking into account that the resistivity calculated from the fit is an average value determined from frequency dependent measurements between 1 and 100 Hz. Therefore eddy current contributions are also included here.

5. Summary

The results of this thesis can be summarised as follows:

- A procedure to measure hystereses with triangular B -field was successfully implemented and tested for ring shaped samples with different hysteresis characteristics.
- The implemented procedure is of iterative nature and works faster the softer the material, the lower the maximum B -field and the less frequency dependent the initial measurements with triangular H -field are.
- The simple loss separation ansatz

$$\frac{P}{f} = C_0 + C_1 \cdot f + C_2 \cdot \sqrt{f}$$

EQ. 48

captures the separation of the losses according to

$$P(t) = P_{hyst}(t) + \frac{\sigma d^2}{12} \left(\frac{dJ}{dt} \right)^2 + \sqrt{\sigma G A V_0} \left| \frac{dJ}{dt} \right|^{\frac{3}{2}}$$

EQ. 49

in a satisfying manner where the model becomes valid. It can be used to predict the frequency dependence of the losses for common soft magnetic materials like transformer steel.

- The best results are indeed obtained for transformer steel and a triangular $B(t)$
- The parameter $\sigma d^2/12$ may be obtained from a least square-fit of the frequency dependent averages $\overline{(\partial_t J)^2}$ and $\overline{|\partial_t J|^{3/2}}$ to the dynamic losses P_W and can be used to calculate an estimate of the specific electrical conductivity σ respectively the specific electrical resistivity ρ .

What exceeded the work of this thesis and may be improved in future work, is summarized below:

- Extremely soft magnetic and high permeable samples need better treatment because of their sensitivity to the signal to noise ratio and the high inductivity that is a direct consequence of the high permeability.
- What can be done about samples with high permeability is simply to buy a stronger power amplifier that tolerates higher inductivities. This would also open up the possibility to investigate not so high permeable samples closer to saturation.
- What can be done about extremely noise sensitive samples is a little more tricky than just buying a low-noise amplifier. It is of great importance that the voltage supply of the power amplifier as well as the power amplifier itself should be as low-noise as possible. It may even be necessary to design a special sample holder with optional magnetic shielding for samples as soft as VP800-2 is to enable more accurate loss coefficients using the loss separation there.

Another possible set up is to use one thick wire going through the hole of the ring shaped sample in order to produce the magnetizing field. In this case the sample holder may exploit the fact, that the H -field around a straight wire is of radial symmetric nature and decreases with $1/r$ from the wire centre and thusly generates a field along a circle of this radius that equals a coil of a mean magnetic path length $l_m = 2\pi r$ with a primary winding number $N_1 = 1$. Also the sample holder should be designed in such a way, that it can be put into a Mu-metal box that can be grounded additionally.

6. Literature

- [1] wikipedia, "<https://en.wikipedia.org/wiki/Transformer>," wikipedia, 25 06 2015.
[Online]. Available:
<https://en.wikipedia.org/w/index.php?title=Transformer&oldid=668670278>.
[Accessed 01 07 2015].
- [2] H. Novotny, *Elektrodynamik und Relativitätstheorie*, Wien: ITP TU Wien, 2006.
- [3] A. Prechtel, *Vorlesungen über die Grundlagen der Elektrotechnik*, vol. 2, Wien: Springer, 2008.
- [4] G. Bertotti, *Hysteresis in magnetism*, San Diego: Academic Press, 1998.
- [5] R. Boll, *Vacuumschmelze GmbH: Soft magnetic materials*, Berlin: Siemens-Aktien-Ges., [Abt. Verl.], 1979.
- [6] W. Wallisch, *Synthesis and TEM investigation of (Fe,Co)_{2-3B}: A compound for rare free permanent magnets*, Wien: Diplomarbeit TU Wien, 2015.
- [7] K. Küpfmüller, *Theoretische Elektrotechnik*, Berlin, Heidelberg: Springer, 2013.
- [8] G. Fasching, *Werkstoffe für die Elektrotechnik*, Wien: Springer, 2005.
- [9] ÖVE/ÖNORM, *ÖVE/ÖNORM EN 62044-3: Kerne aus weich magnetischen Materialien - Messverfahren - Teil 3: Messungen der magnetischen Eigenschaften im Leistungsapplikationsbereich*, Wien: Austrian Standards, 2002.
- [10] G. Bertotti, "Space-time correlation properties of the magnetization process and eddy current," *Journal of applied physics*, 1983.
- [11] R. H. Pry and C. P. Bean, "Calculation of the energy loss in magnetic sheet materials using a domain model," *Journal of applied physics*, 1985.

- [12] M. Fuger, Entwicklung eines Messsystems zur Datenermittlung weichmagnetischer Materialien für die mathematische Beschreibung mittels Preisachoperator, Wien: Diplomarbeit TU Wien, 2009.
- [13] I. KEPCO, *Instruction manual for KEPCO Model BOP 100-4M*, Flushing: KEPCO, Inc., 1979.
- [14] W. Haager, *Regelungstechnik*, Wien: Hölder-Pichler-Tempsky, 2000.
- [15] H. Dubbel, *Taschenbuch für den Maschinenbau*, Berlin: Springer, 1990.
- [16] S. Hartl, *Magnetic properties of deformed electrical steel*, Wien: Diplomarbeit TU Wien, 2014.
- [17] NI, *DAQ S Series - S Series User Manual*, Austin: National Instruments Corporation, 2009.
- [18] M. Kozek and B. Gross, "Identification and Inversion of Magnetic Hysteresis for Sinusoidal Magnetization," *IJOE*, 2005.
- [19] R. Grössinger, M. Antoni, S. Sorta, M. Palm, J. C. Schuster and K. Hiebl, "Magnetic Properties of Fe_{56.7}Ni₁₀Si_{33.3}," *IEEE Transactions On Magnetics*, vol. 50, no. 4, April 2014.
- [20] H. P. J. [J. Wijn, *Magnetic alloys for technical applications, soft magnetic alloys, invar and elinvar alloys.*, Vols. Group 3, Volume 19, Subvolume I 1, Berlin: Springer, 1994.
- [21] I. Mayergoyz, "Mathematical Models of Hysteresis," *Physical Review Letters*, pp. 1518-1521, 01 05 1986.
- [22] F. Preisach, "Über die magnetische Nachwirkung," *Zeitschrift für Physik*, p. 277, 1935.
- [23] M. Antoni, "Setting up a test stand for hysteresis measurements with

LabVIEW,” Projektarbeit TU Wien, Wien, 2011.

[24] N. Mehboob, Hysteresis properties of soft magnetic materials, Wien:
Dissertation Universität Wien, 2012.

Appendices:

Appendix A: Sample characteristics:

	$Fe_{75}Al_{25}$	$Fe_{97}Si_3$	$Fe_{56.7}Ni_{10}Si_{33.3}$	VP800-2	Unit
Origin of the sample	¹⁵	¹⁵	¹⁶	¹⁷	
d_a	7,66	6,92	56,1	21,62	[mm]
d_i	5,78	5,00	45,0	16,00	[mm]
h	0,47	0,82	5,00	24,76	[mm]
w		0,10662		25,069	[g]
ρ	~ 6000 [20]	7650		7350	$[\frac{kg}{m^3}]$
l_m	21,1	18,7238	158,807	59,093	[mm]
A	0,442	0,7872	27,8	69,576	[mm ²]
k_{Fe}	1	1	1	0,7963	[1]
A_{Fe}	0,442	0,7872	27,8	55,405	[m ²]
N_1	72	94	616	5	[1]
N_2	42	56	161	10	[1]

TAB. 37: SUMMARY OF ALL SAMPLE PARAMETERS FOR THE SAMPLES USED IN THE COURSE OF THIS THESIS

¹⁵ Mehboob, N.; Institut für Festkörperphysik TU Wien [24]

¹⁶ Schuster, J.C.; Hiebl, K.; AG Neue Materialien Universität Wien

¹⁷ Vakuumschmelze Hanau

Appendix B: HysteresisMeasurements.vi: A short user manual

This chapter shall serve as a short guide on how to measure with the LabVIEW program written in the course of this thesis and will be explaining the two major tasks:

- How to demagnetize a sample
- How to measure a hysteresis with either an automatically calculated output voltage or with an output voltage function that is read in from a file.

How to demagnetize a sample

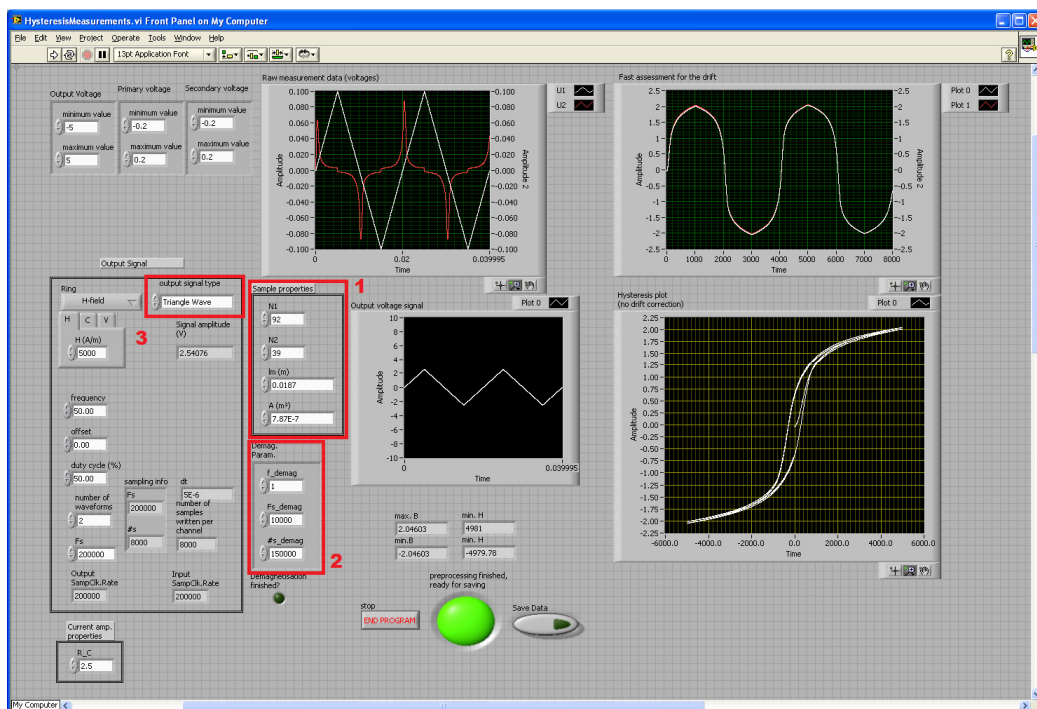


FIG. 51: SCREENSHOT OF THE OPEN BUT NOT RUNNING PROGRAM HYSTERESISMEASUREMENTS.VI

The first thing to do after opening the program is to enter the sample parameters at Fig. 51.1, note that the mean magnetic path length is given in meters and the cross section is the iron cross section in square meters. The iron cross section is the geometrical cross section times the lamination number which is 1 for bulk samples and characterizes the percentage of the cross section being taken up by the material itself for laminated samples. When finished with entering the sample parameters, one just needs to state at Fig. 51.2 which frequency shall be used for how long to demagnetize and set the output function at Fig. 51.3 to “Demag. Sine”.

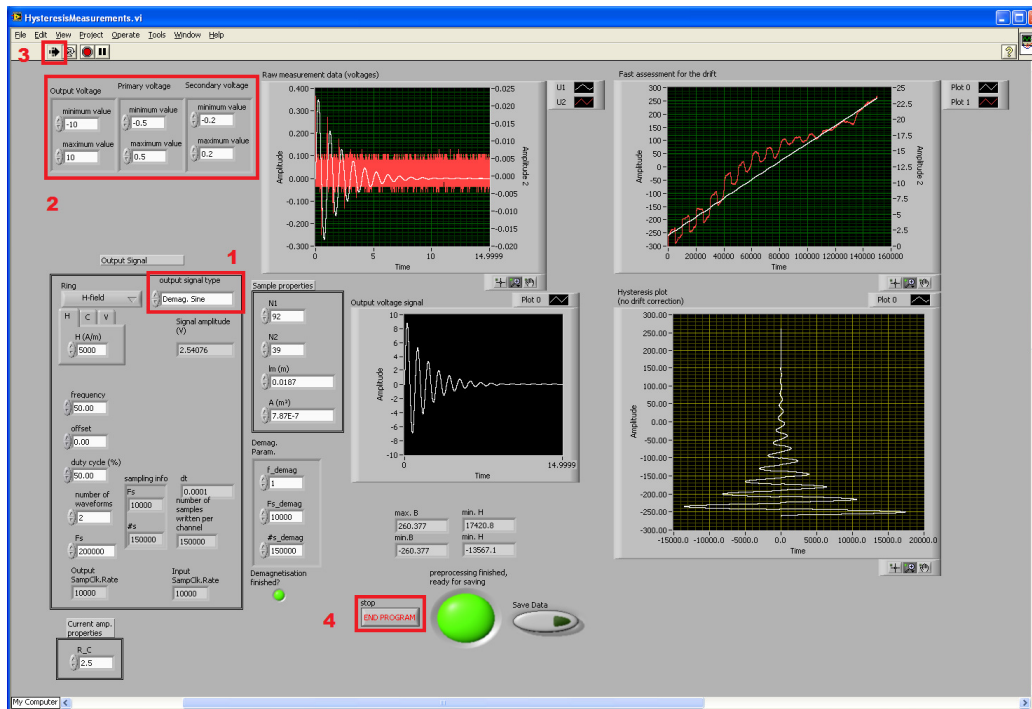


FIG. 52: SCREENSHOT OF THE PROGRAM HYSTERESISMEASUREMENTS.VI AFTER A SUCCESSFUL DEMAGNETIZATION PROCEDURE

After the output function type at Fig. 52.1 is set to “Demag. Sine”, one has to adjust the voltage limits of the input and output channels if need be. After that, the program may be started by clicking start at Fig. 52.3 and ending the program by clicking at the “End program” button at Fig. 52.4.

Empirically it has turned out to be appropriate for most sample types to use the following demagnetization parameters

- Demagnetization frequency: 1 Hz
- Demagnetization duration 15 seconds¹⁸

The frequency and duration may be adjusted in such a manner, that the duration shall be an integer multiple of half the oscillation time of the demagnetization frequency so that the last value put out when the program stops is always zero.

¹⁸ The measurement duration is given by the number of samples to be put out. A sufficient sample frequency is for example 10 kilo-samples per second.

How to measure a hysteresis

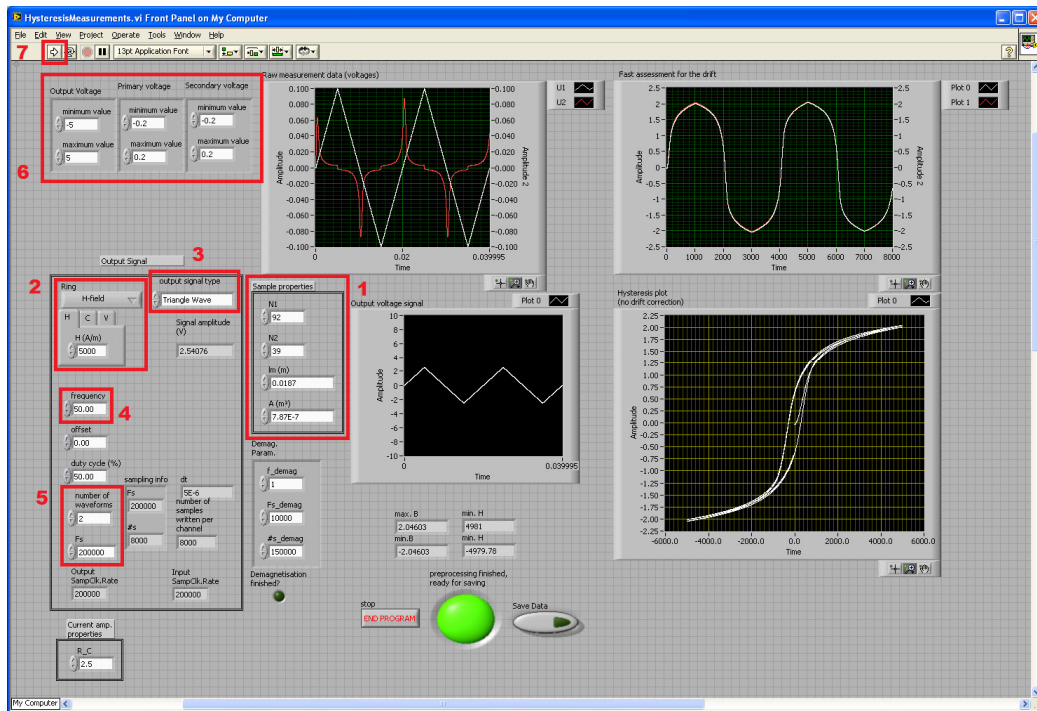


FIG. 53: SCREENSHOT OF THE OPEN BUT NOT RUNNING PROGRAM HYSTERESISMEASUREMENTS.VI

When an actual hysteresis shall be measured, one needs to start similar to the demagnetizing procedure: right after opening the program, one still needs to enter the sample parameters at Fig.53.1. For further information on the units of the sample parameters, see the section on demagnetizing the sample. When finished with entering the sample parameters, one just needs to state at Fig. 53.2 - 5 the measurement conditions (shape, frequency, amplitude and sample rate). As for the triangular B-field, one needs to select "Custom 2" at Fig. 53.3 to read in a two column file supplied in the binary format "*.tdms".

After defining the output and input measurement ranges at Fig. 53.6 the measurement may be started by clicking at Fig. 53.7.

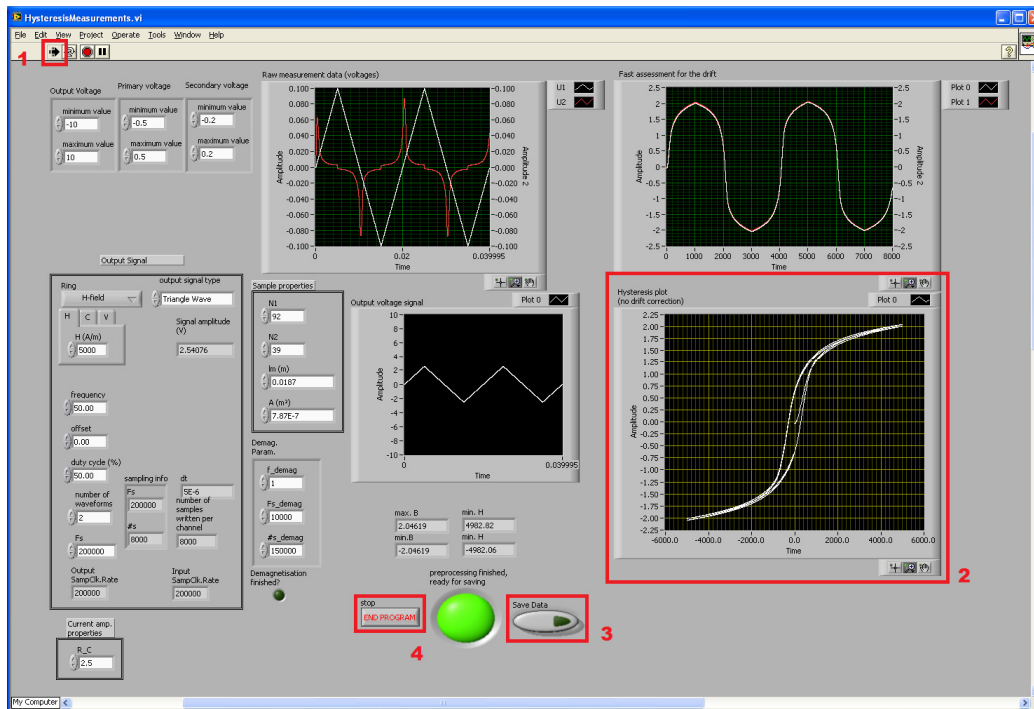


FIG. 54: SCREENSHOT OF THE PROGRAM HYSTERESISMEASUREMENTS.VI AFTER A SUCCESSFUL MEASUREMENT PROCEDURE

After the program is started and has performed the measurement, the preprocessed data (time, current proportional voltage U_1 , B-field-derivative proportional voltage U_2 , H-field and B-field) may be saved via clicking at Fig. 54.3 before ending the program by clicking at Fig. 54.4.

Appendix C: Mathematics of the model comparison process

This chapter shall explain, how the simple loss separation ansatz

$$\frac{P}{f} = C_0 + C_1 \cdot f + C_2 \cdot \sqrt{f}$$

EQ. 50

can be numerically compared to

$$P(t) = P_{hyst}(t) + \frac{\sigma d^2}{12} \left(\frac{dJ}{dt} \right)^2 + \sqrt{\sigma G A V_0} \left| \frac{dJ}{dt} \right|^{\frac{3}{2}}$$

EQ. 51

As already mentioned in Eq. 41, the following assumptions can be made comparing those two equations

$$\begin{aligned} P_{hyst} &= C_0 \cdot f & (a) \\ P_{cl} &= \frac{\sigma d^2}{12} \left(\frac{dJ}{dt} \right)^2 = C_1 \cdot f^2 & (b) \\ P_{exc} &= \sqrt{\sigma G A V_0} \left| \frac{dJ}{dt} \right|^{\frac{3}{2}} = C_2 \cdot f^{\frac{3}{2}} & (c) \end{aligned}$$

EQ. 52

considering, that the losses per cycle P/f equal $P(t)$ multiplied by the frequency f . Formally however, one compares a time dependent function of the time derivative of the magnetic polarization $J(t)$ to a scalar value P/f for each frequency f here.

To truly be able to compare the simple loss separation ansatz to the model describing the losses as a function of the polarization, one has to calculate the time average of $P(t)$ over one cycle respectively one hysteresis loop. The static losses P_H can safely be assumed to equal $C_0 \cdot f$, so one only needs to separate the eddy current and thusly frequency dependent losses P_W into the classical eddy current losses P_{cl} and the excess eddy current losses P_{exc} :

$$\underbrace{P(t)}_{(P/f) \cdot f} = \underbrace{P_H}_{C_0 \cdot f} + \underbrace{P_W}_{P_{cl} + P_{exc}}$$

EQ. 53

To simplify further calculations, let the prefactor in

$$P_{cl} = \underbrace{\frac{\sigma d^2}{12}}_{A_0} \left(\frac{dJ}{dt}\right)^2$$

EQ. 54

be called A_0 and the prefactor in

$$P_{exc} = \underbrace{\sqrt{\sigma G A V_0}}_{A_1} \left|\frac{dJ}{dt}\right|^{\frac{3}{2}}$$

EQ. 55

be called A_1 . All that one needs to do first is to calculate the time average of $(dJ/dt)^2$ and $|dJ/dt|^{3/2}$ according to the following formulas

$$\overline{(\partial_t J)^2} = \underbrace{\frac{1}{T}}_f \int_{t_1}^{t_1+T} (\partial_t J)^2 dt \quad (a)$$

$$\overline{|\partial_t J|^{3/2}} = \underbrace{\frac{1}{T}}_f \int_{t_1}^{t_1+T} |\partial_t J|^{3/2} dt \quad (b)$$

EQ. 56

for each measured frequency f . $\partial_t J$ is the time derivative of J . The following graphs illustrate how this looks for an actual measurement. The measurement that was chosen for illustrating the calculation process of $(dJ/dt)^2$ and $|dJ/dt|^{3/2}$, respectively their time averages $\overline{(dJ/dt)^2}$ and $\overline{|dJ/dt|^{3/2}}$, was the 10 Hz measurement of $Fe_{97}Si_3$ under triangular H-field and is highlighted in the summarizing table below:

f	P/f	$\overline{(\partial_t J)^2}$	$\overline{ \partial_t J ^{3/2}}$	P_W	$C_1(f, A_0)$	$C_2(f, A_1)$
[Hz]	[J/m ³]			[(J/m ³) * s]	[(J/m ³) * s]	[(J/m ³) * s ^{1/2}]
2	766,224	2,013 k	139,484	763,367	33,241	138,577
5	842,786	11,430 k	534,700	2,291 k	30,202	134,389
10	1083,662	41,938 k	1,470 k	6,991 k	27,703	130,650
20	1423,564	151,663 k	4,017 k	20,780 k	25,046	126,218
50	2287,470	808,187 k	14,991 k	95,147 k	21,354	119,146
100	3372,600	2,808 M	40,189 k	298,806 k	18,551	112,932
200	5048,046	9,581 M	106,726 k	932,701 k	15,822	106,031

TAB. 38: COPY OF TAB 32: FREQUENCY DEPENDENT ESTIMATION OF C_1 AND C_2 FOR $Fe_{97}Si_3$ UNDER TRIANGULAR H-FIELD OF AMPLITUDE 20 KA/M FROM PAGE 68

The fit parameters according to Eq. 50 are also needed here:

	Value	Standard Error
C_0	384,5	68,1
C_1	9,11	1,5
C_2	202,5	23,35

TAB. 39: COPY OF TAB 27 FIT PARAMETERS OF THE SIMPLE LOSS SEPERATION ANSATZ OF BERTOTTI FOR $Fe_{97}Si_3$ UNDER TRIANGULAR H-FIELD OF AMPLITUDE 20 KA/M FROM PAGE 67

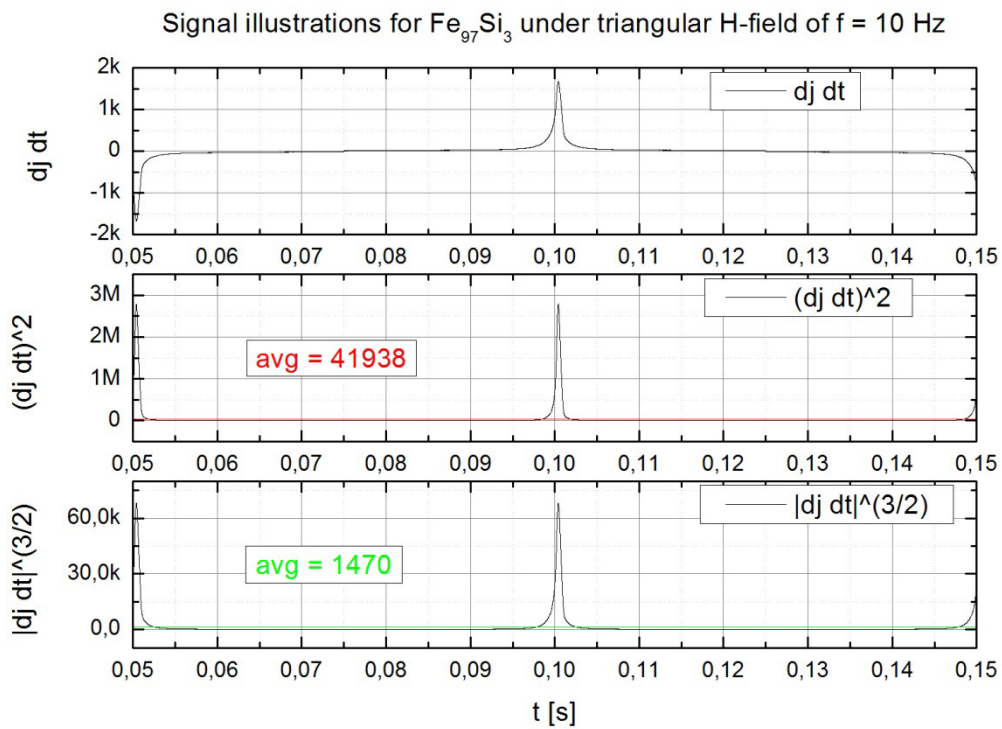


FIG. 55: ILLUSTRATION OF THE AVERAGING PROCESS OF THE TIME DERIVATIVE OF THE MAGNETIC POLARIZATION J FOR $Fe_{97}Si_3$ CAUSED BY TRIANGULAR H-FIELD

If one now calculates the time averages according to Eq. 56 a and b, one arrives at these values

$$\begin{aligned} \overline{(dJ/dt)^2}(f = 10Hz) &= 41938 \\ \overline{|dJ/dt|^{3/2}}(f = 10Hz) &= 1470 \end{aligned}$$

This needs to be done for each frequency, then one can go on to calculate the dynamic losses. This is done according to the following formula:

$$P_W = \left(\frac{P}{f} - C_0 \right) \cdot f$$

EQ. 57

For the 10 Hz measurement, this calculation goes as follows

$$P_W(f = 10Hz) = \underbrace{(1083,662 - 384,54)}_{699,122} \cdot 10 = 6991$$

EQ. 58

and needs to be repeated for each frequency. Now one has three columns: one for the frequency dependent average of $(dJ/dt)^2$, one for the frequency dependent average of $|dJ/dt|^{3/2}$ and one for the frequency dependent eddy current losses P_W . By performing a least square fit one now needs to find the parameters A_0 and A_1 from the following formula for the dynamic losses:

$$P_W = A_0 \underbrace{(\partial_t J)^2}_{"x_0(f)"} + A_1 \underbrace{|\partial_t J|^{3/2}}_{"x_1(f)"}$$

EQ. 59

which can be written as

$$\hat{X} \cdot \vec{A} = \hat{Y}$$

EQ. 60

with the assumption of \hat{X} being a column-matrix with $x_0(f)$ being the values of the first column and $x_1(f)$ being the values of the second column and \hat{Y} being the measurement values of P_W and \vec{A} being the vector that contains the proportionality factors¹⁹ A_0 as first value and A_1 as second value. As \hat{X} and \hat{Y} are defined by the measurement, one needs to calculate a least square fit according to

$$\vec{A} = (X^T X)^{-1} X^T \vec{Y}$$

EQ. 61

to get the parameters A_0 and A_1 .

¹⁹ These prefactors were already mentioned in Eq. 54 and Eq. 55 as well as in Eq. 59.

When one now inserts the respective columns of Tab. 38, one gets the following values for \vec{A}

$$\vec{A} = \begin{pmatrix} A_0 = 66,057 \cdot 10^{-3} \\ A_1 = 2,810 \end{pmatrix}$$

EQ. 62

as was already mentioned in Tab. 36.

Name	A_0	A_1	$\rho(A_0)$
Sinusoidal H-field 20 kA/m	64,560 m	3,001	0,867 $\mu\Omega m$
Triangular H-field 20 kA/m	66,057 m	2,810	0,848 $\mu\Omega m$
Triangular B-field 1,8 T	70,347 m	384,380 m	0,796 $\mu\Omega m$
Triangular B-field 1,7 T	78,574 m	238,839 m	0,713 $\mu\Omega m$
Triangular B-field 1,6 T	79,051 m	431,182 m	0,708 $\mu\Omega m$

TAB. 40: COPY OF TAB.36: LEAST SQUARE FIT PARAMETERS FOR LOSS EVALUATION OF $Fe_{97}Si_3$ UNDER DIFFERENT FIELD SHAPES WITH THE SPECIFIC ELECTRICAL RESISTIVITY RESULTING FROM THE RESPECTIVE A_0 AND THE SLAB THICKNESS

Now one can calculate the last two columns of Tab. 38 respectively Tab. 32 by calculating the following formulas

$$\begin{aligned} C_1(f) &= \frac{1}{f^2} A_0 x_0(f) \\ C_2(f) &= \frac{1}{f^{3/2}} A_1 x_1(f) \end{aligned}$$

EQ. 63

This gives for $f = 10 \text{ Hz}$ under triangular H-field

$$\begin{aligned} C_1(f = 10 \text{ Hz}, A_0 = 66,057 \cdot 10^{-3}) &= \frac{1}{f^2} \cdot 66,057 \cdot 10^{-3} \cdot 41,938 \cdot 10^3 = 27,703 \\ C_2(f = 10 \text{ Hz}, A_1 = 2,810) &= \frac{1}{f^{3/2}} \cdot 2,810 \cdot 1,470 = 130,650 \end{aligned}$$

EQ. 64

and has to be calculated for every frequency.

The last thing one can do now is to calculate the specific electrical conductivity respectively the resistivity. Looking at Eq. 54

$$P_{cl} = \underbrace{\frac{\sigma d^2}{12}}_{A_0} \underbrace{\left(\frac{dJ}{dt}\right)^2}_{x_0(f)}$$

EQ. 65

One sees, that σ and therefore ρ depend only on the known parameters A_0 and A_1 and the thickness d of the sample²⁰:

$$\sigma = \frac{1}{\rho} = \frac{A_0 \cdot 12}{d^2}$$

EQ. 66

which gives the following value for $Fe_{97}Si_3$ at 10 Hz under triangular H-field

$$\rho = \frac{(0,82 \cdot 10^{-3})^2}{66,057 \cdot 10^{-3} \cdot 12} = 0,848 \cdot 10^{-6}$$

EQ. 67

and has the units Ωm . Comparing now the calculated $0,848 \mu\Omega m$ to the well known literature value of the specific electrical resistivity of transformer steel of very similar composition of $\sim 0,4 \mu\Omega m$, this is a very good result, as it matches it to an order of magnitude, deviating from the literature value because one averages over a wide frequency range here to get A_0 .

²⁰ The sample thickness of the $Fe_{97}Si_3$ -sample is 0,82 mm, as can be seen in Tab. 37 on page 74.